HHS Public Access

Author manuscript

Cell Rep. Author manuscript; available in PMC 2019 December 03.

Published in final edited form as:

Cell Rep. 2019 August 13; 28(7): 1879–1893.e7. doi:10.1016/j.celrep.2019.07.044.

Pro-Survival Lipid Sphingosine-1-Phosphate Metabolically Programs T Cells to Limit Anti-tumor Activity

Paramita Chakraborty[1], **Silvia G. Vaena**[2], **Krishnamurthy Thyagarajan**[1], **Shilpak Chatterjee**[1], **Amir Al-Khami**[1], **Shanmugam Panneer Selvam**[2], **Hung Nguyen**[3], **Inhong Kang**[4], **Megan W. Wyatt**[3], **Uday Baliga**[4], **Zachariah Hedley**[1], **Rose N. Ngang**[2], **Beichu Guo**[3], **Gyda C. Beeson**[5], **Shahid Husain**[6], **Chrystal M. Paulos**[3], **Craig C. Beeson**[5], **Michael J. Zilliox**[7], **Elizabeth G. Hill**[8], **Meenal Mehrotra**[4], **Xue-Zhong Yu**[3], **Besim Ogretmen**[2,*], **Shikhar Mehrotra**[1,9,*]

[1]Department of Surgery, Hollings Cancer Center, Medical University of South Carolina, Charleston, SC 29425, USA

[2]Department of Biochemistry and Molecular Biology, Hollings Cancer Center, Medical University of South Carolina, Charleston, SC 29425, USA

[3]Department of Microbiology and Immunology, Medical University of South Carolina, Charleston, SC 29425, USA

[4]Department of Pathology and Laboratory Medicine, Medical University of South Carolina, Charleston, SC 29425, USA

[5]Department of Pharmaceutical and Biomedical Sciences, Medical University of South Carolina, Charleston, SC 29425, USA

[6]Department of Ophthalmology, Medical University of South Carolina, Charleston, SC 29425, USA

[7]Department of Public Health Sciences, Stritch School of Medicine, Loyola University Chicago, Maywood, IL 60153, USA

[8]Department of Public Health, Hollings Cancer Center, Medical University of South Carolina, Charleston, SC 29425, USA

[9]Lead Contact

[*]Correspondence: ogretmen@musc.edu (B.O.), mehrotr@musc.edu (S.M.).

AUTHOR CONTRIBUTIONS

Conception and design, P.C., K.T., B.O., and S.M.; development of methodology, P.C., S.G.V., K.T., S.C., A.A.-K., S.P.S., M.W.W., U.B., R.N.N., H.N., B.G., M.M., S.H., and S.M.; acquisition of data (provided animals, acquired and managed patients, provided facilities, etc.), P.C., K.T., A.A.-K., S.C., I.K., U.B., Z.H., C.M.P., G.C.B., C.C.B., X.Z.Y., B.O., and S.M.; analysis and interpretation of data (e.g., statistical analysis, biostatistics, computational analysis), P.C., S.C., M.M., M.J.Z., and S.M.; writing, review, and/or revision of the manuscript, P.C., K.T., S.C., C.M.P., C.C.B., M.J.Z., M.M., X.Z.Y., B.O., and S.M.; administrative, technical, or material support (i.e., reporting or organizing data, constructing databases), P.C., S.C., E.G.H., B.O., and S.M.; and study supervision, S.M.

SUPPLEMENTAL INFORMATION

Supplemental Information can be found online at https://doi.org/10.1016/j.celrep.2019.07.044.

DECLARATION OF INTERESTS

B.O. and S.M. are co-founders of Lipo-Immuno Tech, LLC. B.O. is the CEO, and S.M. is the CSO at LipoImmunoTech, LLC. C.C.B. is the President and CEO of MitoChem Therapeutics.

SUMMARY

Sphingosine 1-phosphate (S1P), a bioactive lysophospholipid generated by sphingosine kinase 1 (SphK1), regulates lymphocyte egress into circulation via S1P receptor 1 (S1PR1) signaling, and it controls the differentiation of regulatory T cells (Tregs) and T helper-17 cells. However, the mechanisms by which receptor-independent SphK1-mediated intracellular S1P levels modulate T cell functionality remains unknown. We show here that SphK1-deficient T cells maintain central memory phenotype and exhibit higher mitochondrial respiration and reduced differentiation to Tregs. Mechanistically, we discovered a direct correlation between SphK1-generated S1P and lipid transcription factor PPARγ (peroxisome proliferator-activated receptor gamma) activity, which in turn regulates lipolysis in T cells. Genetic and pharmacologic inhibition of SphK1 improved metabolic fitness and anti-tumor activity of T cells against murine melanoma. Further, inhibition of SphK1 and PD1 together led to improved control of melanoma. Overall, these data highlight the clinical potential of limiting SphK1/S1P signaling for enhancing anti-tumor-adoptive T cell therapy.

Graphical Abstract

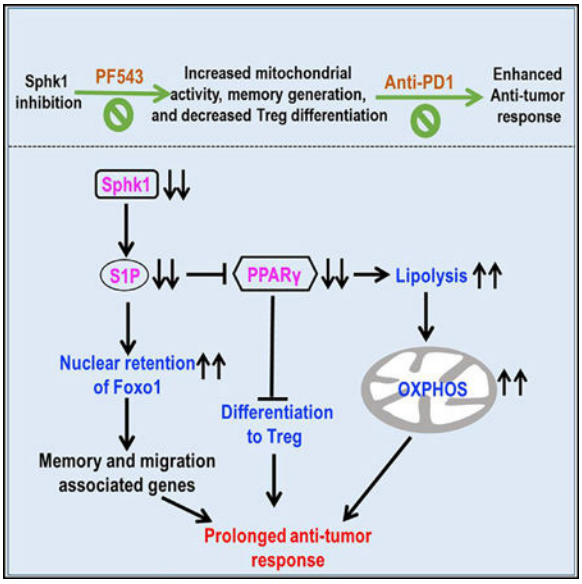

In Brief

Chakraborty et al. define the role for SphK1/S1P signaling via engaging lipid transcription factor PPARγ to attenuate lipolysis and spare respiratory capacity in T cells. Genetic ablation or pharmacological inhibition of SphK1 expression limits intrinsic S1P levels and improves T cell-mediated anti-tumor immunotherapeutic control.

INTRODUCTION

The goal of T cell adoptive immunotherapy for cancer is to make use of the patient's immune system to eliminate malignant cells (Rosenberg and Restifo, 2015). However, programming anti-tumor T cells with the ability to overcome tumor-induced suppression and

metabolically compete with highly glycolytic tumors is key for enhancing persistence and achieving robust tumor control (Chang et al., 2015). Enhanced mitochondrial metabolism and lipolysis, which fuels mitochondrial fatty-acid oxidation, governs metabolic fitness and memory response of the anti-tumor T cells (van der Windt et al., 2012; O'Sullivan et al., 2014). However, how upstream signaling components regulate T cells metabolic commitment toward lipolysis remains unclear.

Sphingosine 1 phosphate (S1P), a bioactive lipid molecule, signals through a family of G-protein-coupled receptors, GPCRs (S1P receptors 1–5, S1PR1–5) to mediate cancer cell growth, proliferation, and/or survival (Chi, 2011; Ponnusamy et al., 2012; Saddoughi et al., 2008). The balance between its synthesis from sphingosine through sphingosine kinases 1 or 2 (SphK1 or SphK2) and its degradation by S1P lyase regulates cellular S1P abundance (Ogretmen, 2018). It is known that the S1P gradient in the plasma plays a major role in the egress of lymphocytes from lymphoid organs to the blood stream via paracrine S1PR1 signaling (Matloubian et al., 2004). S1PR1-induced selective activation of the Akt-mTOR kinase pathway impedes the development and function of regulatory T cells (Treg), suggesting that S1PR1-mTOR axis directs the reciprocal differentiation of Th1 and Treg cells (Liu et al., 2010). Moreover, in addition to receptor-dependent signaling, intracellular S1P regulates various signal transduction pathways by directly binding its targets via lipid-protein interaction (Ogretmen, 2018). For example, while SphK2-generated S1P binds HDAC1/2 (Hait et al., 2009) or telomerase (Panneer Selvam et al., 2015), SphK1-generated S1P binds TRAF2 for nuclear factor κB (NF-κB) activation (Alvarez et al., 2010) or PPARγ for induction of PPARγ-dependent transcription (Parham et al., 2015). While the pro-survival role of S1P in cancer cells has been well studied, its role in modulating T cell metabolism for controlling anti-tumor immune response is not known.

Here, we report that targeting of SphK1 in T cells, and thereby modulating the level of intracellular S1P, alters S1P-PPARγ binding and PPARγ transcriptional activity. Loss of PPARγ activation, in turn, resulted in improved usage of stored lipid in starved conditions and reduced *trans*-differentiation to iTreg phenotype. Furthermore, loss of S1P in *SphK1*$^{-/-}$ T cells led to increased nuclear retention of Foxo1, which in turn enhanced the ability to migrate and render central memory phenotype, resulting in improved anti-tumor T cell response.

RESULTS

Tcm Phenotype in *SphK1*$^{-/-}$ T Cells with Reduced Intrinsic S1P

To determine the role of SphK1/S1P signaling in regulating anti-cancer T cells, we first measured the expression of SphK1 on the tumor infiltrating lymphocytes (TILs) obtained from murine melanoma (B16-F10)-bearing C57BL/6 mice. TILs had a higher expression of SphK1 compared to the splenocytes from the same tumor-bearing mice, indicating that the tumor microenvironment (TME) enhances SphK1 expression (Figure 1A). Thus, we hypothesized that SphK1-mediated S1P may also have a pro-tumorigenic role by altering T cell effector phenotype, and inhibiting SphK1 could be useful for T cell immunotherapy of cancer. To test this hypothesis, we generated *pMel-SphK1*$^{-/-}$ mice by breeding pMel T cell receptor (TCR) transgenic mice that bear the gp100 melanoma epitope-reactive TCR, with

SphK1$^{-/-}$ mice (Figure S1A). We confirmed that expression of transgenic TCR was not affected, and *SphK1* mRNA was undetectable in the splenic T cells obtained from *pMel-SphK1*$^{-/-}$ mice (Figures S1B and S1C). Level of S1P in the *pMel-SphK1*$^{-/-}$ T cells was also reduced (~50%) compared to the wild-type (WT) control (Figure S1D). TCR transgenic T cells and other subsets of immune cells from pMel (-*SphK1*$^{+/+}$) and *pMel-SphK1*$^{-/-}$ mice exhibited a similar phenotype (Figure S1E), suggesting that the reconstitution of the peripheral lymphoid organs was unaffected. No significant difference in the degree of proliferation was measured using carboxyfluorescein succinimidyl ester (CFSE) dilution (Figure 1B), and upregulation of activation markers CD69 and CD25 (Figure 1C) was observed between pMel and *pMel-SphK1*$^{-/-}$ T cells upon TCR stimulation using cognate gp100 peptide for 3 days. Given the role of S1P in T cell migration, we also determined if *pMel-SphK1*$^{-/-}$ T cells exhibit resident memory (Trm) phenotype. Although cell surface marker expression indicative of Trm phenotype was not enhanced (Figure S1F), expression of cell surface marker CD62L that normally decreases with proliferation (Bachmann et al., 2005) was found to be maintained in *pMel-SphK1*$^{-/-}$ T cells as compared to pMel T cells (Figure 1D). Additionally, *SphK1*$^{-/-}$ T cells also exhibited increased cell surface expression of stem cell antigen (Sca1) or CD122 and CD127 (Figure 1E), markers associated with high stem cell memory (Tscm) phenotype and increased tumor control (Gattinoni et al., 2012). The role of SphK1 in rendering Tcm phenotype was confirmed by generating SphK1 chimera (Figure S1G), where a comparison of WT host (CD45.1) and reconstituted *SphK1*$^{-/-}$ (CD45.2) showed a higher CD62L^{+}CD44^{+} fraction (Figure S1H) with enhanced Sca1 expression (Figure S1I).

Because a higher fraction of the *SphK1*$^{-/-}$ T cells exhibited Tcm phenotype, we determined whether the strategy to *ex vivo* generate Tcm cells using interleukin (IL)-15 also leads to decreased SphK1 expression. Thus, we stimulated gp100 reactive pMel CD8^{+} T cells in IL-2 for 3 days and then differentially cultured the cells in IL-2 or IL-15 for 4 more days to program T effector and T memory cells (Figure 1F), respectively (O'Sullivan et al., 2014; van der Windt et al., 2012). We observed that IL-15 cultured T memory cells (with increased CD62L expression) showed decreased levels of SphK1, as compared to the IL-2 cultured T effector cells (Figure 1G). Importantly, overexpressing SphK1 in activated T cells treated with IL-15 led to reduced CD62L expression (Figure 1H, left panel), along with concomitant increase in total lipid content (Figure 1H, right panel). Further, the increased SphK1 expression in TILs (in Figure 1A) could be explained by the enhanced levels of SphK1 that were observed when T cells were cultured with transforming growth factor β (TGF-β) (Figures 1H and S1J), an immunosuppressive cytokine abundantly found in TME. These data indicate that SphK1 may play an important role in deciding the T cell memory phenotype and function in a TME.

Activated *SphK1*$^{-/-}$ T Cells Secrete Both IFN-γ and IL-17 and Exhibit Increased Tumor Control

Upon antigen restimulation, interferon-gamma (IFN-γ), an important anti-tumor effector cytokine secreted by T cells during activation, was similar between the pMel and *pMel-SphK1*$^{-/-}$ T cells (Figure 2A). Surprisingly, *pMel-SphK1*$^{-/-}$ T cells secreted high levels of IL-17 without undergoing any *ex vivo* programming (Figure 2B). Increased secretion of

IL-17 was also confirmed using the multiplex cytokine bead array (Figure S2A), which was consistent with higher expression of Th17-associated transcription factors RORγ and IRF4 (Figure 2C). Additionally, T cells from *SphK1*$^{-/-}$ IL-17-GFP reporter mice showed enhanced IL-17 transcription as compared to WT T cells after Th17 polarization (Figure 2D). *pMel-SphK1*$^{-/-}$ T cells also exhibited increased abundance of "self" immunity-related pathogenic genes, such as *IL9*, *IL22*, *IL23R*, and *CSF2* (Figure S2B), as well as various stemness-associated genes, such as *Tcf7*, *Lef1*, and *Nanog*, some of which are known to be increased in Th17 cells (Wei et al., 2012) (Figure 2E). To determine if *SphK1*$^{-/-}$ T cells are able to withstand tumor immunosuppression, we compared the effector T cell function after *ex vivo* exposure to TGF-β (Yang et al., 2010), a major immunosuppressive cytokine present in TME. While 48 h exposure to TGF-β resulted in decreased IFN-γ secretion by pMel T cells (Figure S2Ci, upper panel) from 57% to 37%, the IFN-γ secretion by *pMel-SphK1*$^{-/-}$ T cells remained unaffected (64% to 70%) (Figures S2Ci, lower panel, and S2Cii). Further, *ex vivo* differentiation of *SphK1*$^{-/-}$ T cells to induced T regulatory cells (iTregs) not only showed a decrease in FoxP3 expression levels (Figure S2Di) but also a reduction in number of iTregs as compared to WT T cells (Figure S2Dii). Thus, these data suggest that loss of SphK1 in T cells results in attenuation of FoxP3 expression, which could contribute to maintenance of robust effector function in TME.

Next, we checked if *SphK1*$^{-/-}$ T cells exhibit improved anti-tumor response. Thus, we adoptively transferred activated T cells (intravenously [i.v.]) from the pMel or *pMel-SphK1*$^{-/-}$ transgenic mice into B16-F10 solid tumor-bearing C57BL/6 mice. We observed that tumor growth was significantly slower upon adoptive transfer of *pMel-SphK1*$^{-/-}$ T cells, as compared to the mice that received pMel T cells (Figure 2F). Pharmacological inhibition of SphK1 using a small molecule inhibitor PF543 (Schnute et al., 2012) during activation of pMel T cells *ex vivo* also resulted in improved control of B16-F10 melanoma after adoptive T cell transfer, as compared to the untreated pMel T cells (Figure S2E). Similar to *pMel-SphK1*$^{-/-}$ T cells, pMel T cells treated with PF543 showed reduced S1P accumulation (Figure S2F), retained CD62L expression after 3 days of activation (Figure S2G), exhibited enhanced Tscm phenotype (Figure S2G), and increased IL-17 secretion (Figure S2H). A quantitative increase in antigen reactive T cells (Figure 2G, upper panel) with higher cytokine secreting ability (Figure 2G, lower panel) was also observed either with adoptively transferred *pMel-SphK1*$^{-/-}$ T cells or pMel T cells pre-treated with PF543. Consistent with these findings, *pMel-SphK1*$^{-/-}$ T cells showed increased homing to the spleen, lymph nodes, and liver after 48 h of adoptive transfer into *Rag1*$^{-/-}$ mice (Figure 2H). However, TILs obtained from tumors at the experimental endpoint displayed comparable PD1 expression as WT pMel T cells (Figure S2J). Therefore, we checked if combining anti-PD1 with SphK1 inhibition could further improve tumor control. We observed that inhibition of SphK1 with PF543, along with PD1 blockade using anti-PD1 antibody, resulted in long-term control of solid melanoma (Figure 2I, p value for pMel + PF543 versus pMel + PF543 + αPD1 is 2e–06, and p value for pMel + αPD1 versus pMel + PF543 + αPD1 is 3e–07). Thus, this combinatorial strategy, which reduces the intrinsic S1P levels along with checkpoint inhibition, has the potential to be translated to the clinics.

Given that S1P could be generated by both SphK1 (cytoplasmic) and SphK2 (nuclear) (Ogretmen, 2018), we also tested if targeting SphK2 would result in similar T cell phenotype

and enhanced tumor control. Surprisingly, *Pmel-SphK2*$^{-/-}$ T cells neither exhibited high Tcm (CD62L^{hi}CD44^{hi}) phenotype (Figure S3A) nor showed higher expression of Sca1, CD122, and CD127 (Figure S3B). The ability to control B16 murine melanoma was also unchanged (Figure S3C). This suggests a differential role of S1P based on its localization.

SphK1$^{-/-}$ T Cells Exhibit Increased Recall Response

To determine if *SphK1*$^{-/-}$ T cells have enhanced capacity to establish memory *in vivo*, we adoptively transferred 3-day antigen-activated pMel or *pMel-SphK1*$^{-/-}$ T cells into *Rag1*$^{-/-}$ mice. After 25 days, the recipient mice were injected with murine melanoma B16-F10 cells. After 5 days of tumor injection, *pMel-SphK1*$^{-/-}$ T cells exhibited higher recall response to tumor challenge as compared to pMel T cells, as evident from their ~2-fold higher expansion in each organ except lungs (Figure 3A). *SphK1*$^{-/-}$ T cells also displayed reduced expression of exhaustion molecule KLRG1 and increased CD62L expression as compared to WT T cells (Figure 3B). These data support that inhibiting SphK1 expression could result in increased persistence and migration of anti-tumor T cells to lymphoid and non-lymphoid organs.

Next, we examined the mechanism by which loss of SphK1 enhances memory generation and migration in T cells. Recent studies have demonstrated the importance of *Foxo1* in regulating memory-associated marker genes (CD62L and Tcf7) and migration of CD8^{+} T cells (Hess Michelini et al., 2013). Foxo1 activity is mainly regulated by its phosphorylation through Akt kinase activity, which promotes its nuclear export, resulting in a loss of transcriptional activity (Chatterjee et al., 2018). We observed decreased Foxo1 phosphorylation in *SphK1*$^{-/-}$ T cells compared to WT T cells (Figure 3C), which was increased upon adding S1P to the *SphK1*$^{-/-}$ T cells (Figure 3C). Given the role of S1P to activate the Akt pathway (Bonnaud et al., 2010), we hypothesized that S1P-mediated activation of Akt leads to differences in Foxo1 phosphorylation and down-stream signaling pathways to tune *SphK1*$^{-/-}$ T cells with potent anti-tumor phenotype. Indeed, *SphK1*$^{-/-}$ T cells exhibit reduced phosphorylation of Akt upon TCR stimulation, and addition of S1P did result in increased pAkt kinetics in *SphK1*$^{-/-}$ T cells (Figure S3D). Subcellular localization of Foxo1, detected by immunofluorescence and immunoblot analysis, was consistent with its phosphorylation status, showing a higher nuclear abundance in *SphK1*$^{-/-}$ T cells compared to WT T cells (Figures 3D, and S3E). Interestingly, addition of S1P to the media increased nuclear export of Foxo1 in *SphK1*$^{-/-}$ T cells (Figure 3D, right panel). Furthermore, WT T cells treated with Akt inhibitor (Akti) showed reduced phosphorylation of Foxo1, whereas *SphK1*$^{-/-}$T cells cultured in presence of Akt inducer SC-79 exhibited increased phosphorylation of Foxo1 as compared to *SphK1*$^{-/-}$ T cells (Figures S3F and S3G). This indicates that Akt pathway facilitates nuclear retention of Foxo1 in *SphK1*$^{-/-}$ T cells. The role of SphK1 to regulate Foxo1 activity was also confirmed when addition of S1P resulted in diminished Foxo1 activity (Figure 3E). Nuclear localization of Foxo1 also exhibited increased expression of its downstream target *S1PR1* (Gubbels Bupp et al., 2009) in *SphK1*$^{-/-}$ T cells as compared to WT controls (Figure 3F). Importantly, Foxo1 inhibitor AS1842856, blocked the expression of downstream *Foxo1* targets such as CD62L (Figure 3G) and S1PR1 (Figure 3H) in *SphK1*$^{-/-}$ T cells, confirming the role of Foxo1 in *SphK1*$^{-/-}$ T cell memory phenotype.

SphK1$^{-/-}$ T Cells Preferentially Depend on Oxidative Phosphorylation and Lipolysis for Energy Generation

Cell-intrinsic lipolysis fuels mitochondrial respiration and has been implicated in stable Tcm phenotype (O'Sullivan et al., 2014). Because *SphK1*$^{-/-}$ T cells exhibit increased Tcm phenotype, we next evaluated their metabolic programming compared to WT T cells. There were no detectable differences in extracellular acidification rate (ECAR) (a marker of glycolysis) between WT and *SphK1*$^{-/-}$ T cells (Figure 4A). However, the oxygen consumption rate (OCR), an indicator of mitochondrial OXPHOS, was strikingly higher in *SphK1*$^{-/-}$ T cells as compared to WT T cells (Figure 4B). Because fatty acid oxidation (FAO) modulates OXPHOS by providing acetyl-CoA, a substrate for TCA cycle (Stephens et al., 2007), we assessed the contribution of FAO to maintain increased OXPHOS in *SphK1*$^{-/-}$ T cells. We found that *SphK1*$^{-/-}$ T cells showed an increase in carnitine palmitoyltransferase 1 (CPT1a) expression (Figure 4C), the rate-limiting enzyme that regulates fatty acid (FA) entry from cytosol to mitochondria (Stephens et al., 2007). Moreover, inhibition of CPT1a using etomoxir significantly depleted OCR values in *SphK1*$^{-/-}$ cells (Figure 4B). The increased OXPHOS in *SphK1*$^{-/-}$ T cells was also supported by enhanced ATP generation (Figure 4D) and higher mitochondrial number as determined by transmission electron microscopy (Figure S4A). The RNA-sequencing (RNA-seq) analysis also showed that the genes associated with mitochondrial electron transport chains were upregulated in *SphK1*$^{-/-}$ T cells compared to WT T cells (Figure S4B). Because memory T cells use long-chain fatty-acid (FA) to enrich mitochondrial respiration (van der Windt et al., 2012), we investigated if there are any differences in the FA uptake between the WT and *SphK1*$^{-/-}$ T cells. *SphK1*$^{-/-}$ T cells exhibited the decreased ability for the uptake of long chain FA (Figure 4E, left panel), which was consistent with reduced expression of fatty acid translocase (FAT) CD36 compared to WT T cells (Figure 4E, right panel). This suggests that *SphK1*$^{-/-}$ T cells do not depend on the extracellular FA uptake to meet their energy needs. Next, we checked if *SphK1*$^{-/-}$ T cells utilized their own lipid reserves to feed the mitochondrial respiration. To test this, we cultured 3-day activated WT and *SphK1*$^{-/-}$ T cells in complete media, oleic acid (positive regulator of lipid droplet formation) supplemented media, or oleic acid supplemental media followed by 24 h starvation in low glucose media. In response to starvation, *SphK1*$^{-/-}$ T cells preferentially utilized their stored lipids in lipid droplets, compared to WT T cells (Figures 4F, blue overlay, and S4C). Additionally, expression of Tip47, a lipid droplet-associated protein important for lipid droplet biogenesis, was reduced in *SphK1*$^{-/-}$ T cells (Figure 4G). Further, determination of different target molecules involved in lipolysis showed that triglyceride and cholesterol contents were not different in WT and *SphK1*$^{-/-}$ T cells. However, diacylglycerol (DAG) content was largely decreased in *SphK1*$^{-/-}$ T cells (Figure 4H), indicating increased lipolysis in *SphK1*$^{-/-}$ T cells as compared to WT T cells. Expression of lysosomal lipase (*Lipa*), which is capable of hydrolyzing DAG to generate free FA and cholesterol in lysosomes and has been shown to be critical for T memory cells (O'Sullivan et al., 2014; Qu et al., 2009), was also increased in *SphK1*$^{-/-}$ T cells (Figure S4D). Collectively, these data suggest that *SphK1*$^{-/-}$ T cells are more efficacious in utilizing endogenous lipids to fuel FAO, corroborating with their increased survival in a nutrient-deprived TME compared to WT cells.

To further confirm the role of lipolysis-dependent energy generation of *SphK1*$^{-/-}$ T cell, we cultured TCR-activated T cells (WT and *SphK1*$^{-/-}$) for an additional 48 h in the presence of lipolysis pathway inhibitor (orlistat) and determined its effects on their survival. While the viability of the WT T cells remained unaltered, *SphK1*$^{-/-}$ T cells exhibited reduced viability after orlistat treatment (Figure 4I). Decreased IFN-γ secretion (Figure 4J) and reduced OCR in *SphK1*$^{-/-}$ T cells upon orlistat treatment (Figure 4K) was also noticed. Importantly, inhibiting lipolysis hampered the anti-tumor property of *SphK1*$^{-/-}$ T cells upon adoptive transfer (Figure 4L). Thus, metabolic reprogramming for increased lipolysis plays a key role in increased Tcm phenotype and anti-tumor function exhibited by *SphK1*$^{-/-}$ T cells.

S1P-PPARγ Axis Regulates Increased Lipolysis in *SphK1*$^{-/-}$ T Cells

Next, we sought to determine how loss of SphK1 induces lipolysis in *SphK1*$^{-/-}$ T cells. One of the key transcription factors that regulates lipid mobilization, and thereby lipolysis, is PPARγ (Lee and Evans, 2002). Activation of PPARγ also inhibits cytokine response, including IL-17 (Clark et al., 2000; Jones et al., 2002; Klotz et al., 2009; Zhang et al., 2012), and promotes Treg generation (Wohlfert et al., 2007). Recently, SphK1-generated S1P was shown to be a direct PPARγ-activating ligand in human endothelial cells (Parham et al., 2015). Thus, we hypothesized that SphK1-mediated S1P regulates PPARγ activation, which in turn metabolically programs T cell differentiation to effector or regulatory phenotype. Indeed, we observed that *SphK1*$^{-/-}$ T cells and WT T cells treated with PF543 had reduced PPARγ expression as compared to the WT T cells (Figure 5A). Importantly, PPARγ activity was also lower in *SphK1*$^{-/-}$ T cells (Figure 5B). However, activity of another PPAR family member, PPARa, was not significantly different between WT and *SphK1*$^{-/-}$ T cells (Figure 5C). Furthermore, exogenous addition of S1P to the *SphK1*$^{-/-}$ T cells resulted in an increase in PPARγ levels (Figure 5D), suggesting that SphK1-generated S1P directly controls PPARγ expression and/or activity. To assess if altering the PPARγ abundance and/or activity in WT or *SphK1*$^{-/-}$ T cells modulate their function in terms of IL-17 secretion and Foxp3 expression, known targets of PPARγ, we activated the T cells in the presence/absence of thiazolidinedione (TZD) or GW9662, pharmacologic activator or inhibitor of PPARγ, respectively (Panigrahy et al., 2002; Seargent et al., 2004). While activation of PPARγ by either TZD or S1P decreased IL-17 secretion in *SphK1*$^{-/-}$ T cells, inhibition of PPARγ with GW9662 enhanced IL-17 secretion in WT T cells (Figure 5E). To further explore the functional consequence of S1P-mediated PPARγ activation, we evaluated the effects of S1P exposure on FoxP3 expression and IL-17 production in Treg and Th17 polarizing conditions, respectively. *SphK1*$^{-/-}$ T cells cultured in presence of S1P showed reduced levels of IL-17 (Figure 5F; right), and enhanced FoxP3 expression (Figure 5G; right). Together, our data indicate that reduced S1P levels upon SphK1 inhibition attenuates PPARγ activation, preserves IL-17 secretion, and reduces *trans*-differentiation to iTregs.

To confirm if S1P-mediated increase in PPARγ activity is dependent on intrinsic S1P levels, *SphK1*$^{-/-}$ T cells were transfected with vectors containing WT or catalytically inactive mutant SphK1 due to G82D conversion (Bonder et al., 2009; Hait et al., 2005) (Figure 5H, left panel). The data revealed that ectopic expression of WT, but not inactive SphK1, induced PPARγ (Figure 5H, middle panel) and FOXP3 expression (Figure 5H, right panel) and reduced IL-17 secretion (Figure 5I), supporting the role of SphK1-generated S1P in

regulating PPARγ activity in T cells. To check if direct S1P binding leads to PPARγ activation, we generated vectors expressing WT versus mutant PPARγ with altered S1P binding due to H323A conversion, localized within PPARγ ligand binding domain, known to be key for binding to S1P (Parham et al., 2015). *SphK1*$^{-/-}$ T cells were then transduced with either WT-PPARγ (PPARγ^{wt}) vector or H323A-PPARγ mutant (PPARγ^{mut}) vector (Figure S5A). Overexpression of PPARγ in *SphK1*$^{-/-}$ T cells resulted in increased FoxP3 expression (Figure S5B) and decreased IL-17 secretion (Figure S5C). Adding S1P to the culture medium of PPARγ^{wt} expressing *SphK1*$^{-/-}$ T cells further enhanced PPARγ activity, but did not show any significant effect on PPARγ^{mut} expressing *SphK1*$^{-/-}$ T cells (Figures S5B and S5C). This supports a role of direct S1P binding in PPARγ-mediated signaling in T cells. Additionally, we used a similar strategy to determine if PPARγ activation by S1P would lead to differences in lipid mobilization in T cells. We found that fat mobilization in response to starvation is significantly less in *SphK1*$^{-/-}$ T cells containing either PPARγ^{wt} or PPARγ^{mut} vector, as compared to the cells that express PPARγ^{empty} vector only (Figure S5D; Data S1A). However, after S1P addition, we did not detect any further decrease (from the base line) in fat mobilization in either PPARγ^{wt} or PPARγ^{mut} vector expressing *SphK1*$^{-/-}$ T cells (Figure S5D; Data S1A), suggesting that PPARγ overexpression is itself adequate to block the lipid utilization to its maximal level. Last, we asked if there is any role of S1P1 receptor signaling that contributes to the phenotype observed with *SphK1*$^{-/-}$ T cells. However, we observed that despite blocking S1PR1 using FTY720 and W146 and S1PR2 with JT013, S1P was able to exert its effect in terms of reducing IL-17 (Figures S5E and S5G; Data S1B and S1D) and increasing FoxP3 (Figures S5F and S5H; Data S1C and S1E) along with PPARγ expression (Figures S5 and S5J; Data S1F and S1G). This indicates a receptor-independent role of S1P mediated through PPARγ.

PPARγ$^{-/-}$ T Cells Show Enhanced Anti-tumor Potential

In order to confirm the physiological relevance of SphK1-PPARγ axis, we isolated TILs from large B16-F10 tumors established in WT and *SphK1*$^{-/-}$ mice and determined expression of PPARγ and FoxP3. We found that compared to WT TILs, *SphK1*$^{-/-}$ TILs showed reduced expression of both PPARγ and FoxP3 (Figure S6A). Importantly, the physiological relevance of targeting SphK1-PPARγ axis was also evident from unbiased screening of TCGA data, which showed that high SphK1 and PPARγ expression associates significantly with poor survival in patients with various solid tumors, which could suggest their overexpression in infiltrating T cells, including glioblastoma and liver cancers (Figures S6B–S6E). Similar trends were also observed in data obtained from patients with breast, colon, lung, and skin cancer (data not shown). Thus, to determine if reduced PPARγ expression/activity in tumor-reactive T cells will enhance tumor control upon ACT, we characterized the *PPARγ*$^{-/-}$ T cells (obtained after breeding *PPARγ*$^{fl/fl}$ mice with *CD4*^{Cre} mice) *in vitro* and *in vivo*. Similar to *SphK1*$^{-/-}$ T cells, *PPARγ*$^{-/-}$ T cells also exhibited increased expression of Sca1, CD122, and CD127 (Figure 6A), comparable ECAR (Figure 6B) and higher OCR (Figure 6C), indicating higher mitochondrial respiration. To confirm if the enhanced OCR in *PPARγ*$^{-/-}$ T cells is dependent upon cell intrinsic lipolysis, we cultured TCR-activated T cells (WT and *PPARγ*$^{-/-}$) in the presence of orlistat. In the presence of orlistat, *PPARγ*$^{-/-}$ T cells showed lower OCR value (Figure 6C), and lower viability compared to WT control (Figure 6D). Similar to *SphK1*$^{-/-}$ T cells, *PPARγ*$^{-/-}$ T

cells also have a lower expression of CD36 (Figure 6E, left panel) and uptake a less amount of long chain FA from external environment (Figure 6E, right panel) compared to WT cells. Moreover, *PPARγ*$^{-/-}$ T cells rely on their endogenous lipid source to survive in starved condition (Figure 6F)–confirming the role of intrinsic lipolysis to fuel mitochondrial respiration in *PPARγ*$^{-/-}$ T cells. Importantly, T cells activated in presence of IL-15 exhibited lower PPARγ levels, while PPARγ expression was increased in presence of TGF-β (Figures S6F and S6G). These data identify PPARγ as an important regulator in shaping T cell memory and trans-differentiation to iTregs in TME. Further, *PPARγ*$^{-/-}$ T cells engineered with melanoma epitope tyrosinase reactive TCR TIL1383I exhibited improved long-term control of the murine melanoma B16-A2 upon adoptive transfer (Figure 6G). Finally, we observed that overexpressing SphK1 in activated WT T cells (Figure S6H, left panel) led to an increase in PPARγ expression, even in presence of IL-15 (Figure S6H, right panel). This suggests that inhibition or loss of PPARγ results in metabolic reprogramming of T cells by inducing lipolysis and mitochondrial respiration, and an inverse correlation exists between PPARγ and robust anti-tumor T cell phenotype.

DISCUSSION

Sphingolipids have emerged as bio-effector molecules, which control various aspects of cancer cell growth, proliferation, and anti-cancer therapeutics (Saddoughi et al., 2008). However, the mechanisms that regulate the peripheral T cell function through intracellular modulation of SphK1/S1P signaling have been largely understudied. Here, our data reveal an immunometabolic role for SphK1-generated S1P in peripheral T cells through regulation of PPARγ, which represses lipolysis-dependent energy generation and can be targeted genetically or pharmacologically to improve anti-tumor immunity.

Various T cell subsets (effector, memory, regulatory) require distinct energetic and biosynthetic pathways to support their specific functional needs (Al-Hommrani et al., 2016; Buck et al., 2015). Given our data, which show that *pMel-SphK1*$^{-/-}$ T cells secrete both IFN-γ (Tc1) and IL-17 (Tc17), our goal was to understand the mechanism that leads to increased tumor control due to reduced SphK1/S1P signaling in T cells. It has been shown that S1P stimulates Foxo1 phosphorylation and nuclear export by activating PI3K/Akt pathways (Hsu et al., 2015), and moreover, Foxo1 *trans* represses PPARγ activity (Fan et al., 2009). Consistent with these findings, we show that reduced pAkt and pFoxo levels in absence of S1P in *SphK1*$^{-/-}$ T cells lead to higher Foxo1 activity, which simultaneously increased expression of downstream Foxo1 targets such as CD62L and S1PR1. It has also been shown that S1P is an activator of Akt/ mTOR cell survival pathway in different cancer cell types (Bouquerel et al., 2016; Xu et al., 2018). Perhaps two distinct signaling mechanisms (i.e., survival and self-renewal) operate depending on the S1P level, cell types, and environmental stimuli. Understanding how intracellular S1P level regulates survival and self-renewal mechanisms in different cell types and what is the role of cellular microenvironment to activate or inhibit SphK1 enzyme, which in turn controls intracellular S1P abundance, could be a subject of future study.

Another layer of regulation mediated by S1P levels was PPARγ activity, which was attenuated in *SphK1*$^{-/-}$ cells due to lack of direct S1P-PPARγ binding. While higher nuclear

localization of Foxo1 in *SphK1*$^{-/-}$ CD8^{+} T cells increases Tcm phenotype, and potentially contributes to the robust recall responses, attenuation of PPARγ activity render these cells with the enhanced ability to use their stored lipid content even in starved condition. Importantly, *in vitro*-generated T memory cells using IL-15 exhibit reduced SphK1 levels, and overexpressing SphK1 results in loss of CD62L, enhanced lipid content, and higher PPARγ levels. This indicates that SphK1 may have an important upstream role in the generation of memory T cells, which have been shown to rely upon endogenous lipids (O'Sullivan et al., 2014). How IL-15 inhibits SphK1 expression is an intriguing question, because both IL-15 and SphK1-generated S1P have pro-survival roles. However, it is likely that lower oxidative stress due to IL-15 results in reduced activation of SphK1 and dampens the S1P-PPARγ signaling (Kaur et al., 2011; Van Brocklyn and Williams, 2012). Our finding that TGF-β signaling enhances SphK1 expression in T cells complements studies from several other groups in different cell types (Stayrook et al., 2015; Yamanaka et al., 2004), and calls for future studies to delineate this pathway to modulate the immunosuppressive network in TME. We also found that S1P binding to PPARγ regulates downstream signaling in terms of FoxP3 expression. Given the close metabolic commitment of the memory T cells and Tregs on lipid metabolism (Newton et al., 2016), our data suggest that SphK1-generated S1P acts as a switch that decides between the Treg (PPARγ^{hi}) versus Tcm (PPARγ^{lo}) phenotype. Therefore, a novel axis involving S1P-PPARγ can be envisioned in T cells.

PPARγ is a nuclear receptor that combines the features of both transcription factors and receptor molecules, which has the unique ability to bind lipid signaling molecules and transduce the appropriate signals derived from lipid environment to the level of gene expression (Kim et al., 2015). In response to starvation, repression of PPARγ activity reduces the expression of genes that drive fat storage and helps to release free FAs (Picard et al., 2004; Tamori et al., 2002). PPARγ activates genes associated with transport of FA across the plasma membrane (CD36 and FABP4) and those associated with FA storage such as perilipins (Howie et al., 2018). On the other hand, transcription factor Foxo1 controls lipid catabolism/lipophagy via the induction of lipases (such as ATGL and LAL) (Chakrabarti et al., 2011; Lettieri Barbato et al., 2013). Our data show that genetic loss of SphK1 leads to the activation of lipolysis due to downregulation of PPARγ in *SphK1*$^{-/-}$ T cells, whereas restoration of PPARγ led to repression of lipolysis. It is likely that low intrinsic S1P in *SphK1*$^{-/-}$ T cells results in reduced PPARγ activity, whi ch inhibits uptake of exogenous lipids through CD36, and hampers lipid storage through downregulating the expression of Perilipin-3. Thus, one can envisage that in *SphK1*$^{-/-}$ T cells, attenuation of PPARγ activity makes the FA substrates available for utilization, and high Foxo1 activity leads to an increase in lipases that reprogram the metabolic commitment of *SphK1*$^{-/-}$ T cells toward lipolysis. It is likely that owing to their ability to utilize endogenous lipid as fuel, the *SphK1*$^{-/-}$ T cells persist longer in nutrient-deprived TME and result in improved tumor control. In this context, it would be interesting to see if perturbation of S1P level by any other enzyme would endow the T cells with same phenotypic advantages. For example, S1P lyase (SPL) activity results in irreversible hydrolysis of S1P and thus lowers the intracellular level of S1P (Ogretmen, 2018). While S1P lyase in dendritic cells is known to create a S1P gradient *in vivo* and regulate thymic egress (Zamora-Pineda et al., 2016), whether inducing

SPL activity in T cell abrogates intracellular S1P signaling that, in turn, promotes CD62L expression or hampers Treg generation remains to be seen.

Overall, these data have important implications. Pharmacological inhibition of SphK1/S1P or attenuation of PPARγ exhibited similar effects on metabolic reprogramming of T cell in terms of inducing lipolysis due to reduced PPARγ and leading to increased Tcm phenotype with improved anti-tumor activity for ACT. While S1P acts as a pro-survival signal to cancer cells, it also limits the anti-tumor activity of $CD8^+$ T cells in ACT. Identifying metabolic targets that are common to cancer cells and T cells (like S1P) will not only increase the potential of T cell-based anti-cancer immunotherapies, but also pave the way for devising a two-pronged attack on tumors. Thus, this data may have translational value for designing future T cell immunotherapy trials.

STAR★METHODS

LEAD CONTACT AND MATERIALS AVAILABILITY

Further information and requests for resources and reagents should be directed to and will be fulfilled by the Lead Contact, Shikhar Mehrotra (mehrotr@musc.edu). This study did not generate new unique reagents.

EXPERIMENTAL MODEL AND SUBJECT DETAILS

Mice and Tumor Model—C57BL/6, B6-HLA-$A2^+$, B6-$Rag^{-/-}$, Pmel mice were obtained from Jackson Laboratory (Bar Harbor, ME) and used to perform this study. $Sphk1^{-/-}$, $PPAR\gamma^{fl/fl}$ $CD4^{cre}$ mice were a kind gift from Besim Ogretmen (MUSC) and Robert B. Clark (University of Connecticut Health Center), respectively. Pmel-$Sphk1^{-/-}$ mice, $Sphk1^{-/-}$-IL17GFP knock-in mice were developed in the lab. Animals were maintained in pathogen-free facilities, and experimental procedures were approved by Institutional Animal Care and Use Committees of Medical University of South Carolina, Charleston. For tumor experiments, equal number of age- and gender-matched (both male and female) mice were randomly assigned for the experiments when they were between 8–10 weeks old. No influence of sex on the result of the studies was observed.

B16-F10 or B16-F10-$A2^+$ mouse melanoma tumor cells (0.3×10^6) were injected subcutaneously (*s.c.*) into left flank of 8–10 week old C57BL/6 or HLA-$A2^+$ mice respectively. After nine days of tumor establishment, recipient mice were injected *(i.p)* with cyclophosphamide (4 mg/mice) before adoptively transferring (i.v) either Pmel ($CD8^+V\beta13^+$) or TIL1383I TCR^+ cells on day 10. In some experiments, tumor-bearing mice received PF543 (1 mg/Kg; every alternative day; *i.p.*) after adoptive Pmel cells transfer. Recipient mice were given IL2 (50,000 U/mouse; i.p) for three consecutive days after ACT. In few experiments, following ACT, recipient mice were injected (*i.p*) with PF543 (1 mg/kg of body weight, anti-PD1 Ab (200 μg/mouse), or both PF543 and anti-PD1 Ab until day 15, Both PF543 and anti-PD1 Ab were given thrice in a week.

Cell Lines—B16-F10 (RRID: CVCL_0159) was obtained from American Type Culture Collection (ATCC), suggested to be of male origin.

METHOD DETAILS

T Cell Differentiation—Naive total T cells were purified from the total splenocytes of 6–9 week old WT (C57BL/6) and KO (Sphk1$^{-/-}$, PPAR$\gamma^{fl/fl}$CD4^{cre}) mice, first by incubating the cells with biotinylated anti-CD19, anti-CD11b, anti-CD11c, anti-NK1.1, anti-CD25 (cell signaling technology), followed by negative selection with streptavidin magnetic particles (BD Biosciences). Total splenocytes from 6–9 week old TCR transgenic mouse Pmel (bears class-I restricted CD8$^+$ T cells) were also used. Within experiments, mice were age and sex matched. In some experiments, purified naive T cells or total splenocytes were differentiated to Th17 (3 ng/ml TGFβ, 25 ng/ml IL6, 10 μg/ml anti-IL4 and 10 μg/ml anti-IFNγ) and iTreg (5 ng/ml TGFβ, 100 IU/ml IL2, 10 μg/ml anti-IL4 and 10 μg/ml anti-IFNγ or Th0 (100 IU/ml IL2) in presence of plate bound anti-CD3 (5 μg/ml) and anti-CD28 (5 μg/ml). For pmel TCR transgenic mice, splenocytes were stimulated with 1 μg/ml gp100 melanoma antigen in presence of 100 IU/ml IL2. T cells were differentiated for three days in IMDM media supplemented with 10% FCS, 4mM L-glutamine, 100 U/ml penicillin, 100 μg/ml streptomycin, 55 μM beta-mercaptoethanol under 5% CO_2, atmospheric oxygen at 37°C in a humidified incubator. For evaluation of intracellular cytokines by flow cytometry, T cells were re-stimulated either with PMA/ionomycin for four hours, or with plate bound anti-CD3 (5 μg/ml) and anti-CD28 (5 μg/ml) for overnight in presence of Glogi inhibitors. In some experiments, *in vitro* differentiated T cells were either treated with the vehicle control or inhibitor of Sphk1, PF543 (1 μM; added into the differentiation media from day 0) or activator of PPARγ, TZD (100 ng/ml; added into the differentiation media from day 0) or inhibitor of PPARγ (500 nM; added into the differentiation media from day 0), AS1842856 (50nM; added into the differentiation media from day zero) or Orlistat (100 μM; added into the media for 48 hours), or S1P (2 μM, 5 μM or 10 μM; added into the differentiation media from day 0).

Exogenous S1P Treatment—Exogenous S1P (Avanti Polar Lipids) was conjugated with BSA, as described previously (Panneer Selvam et al., 2015). Briefly, S1P was incubated in a sonicator water bath for 5 min followed by incubation at 37° to 55°C for 20 min in methanol. Methanol was evaporated in inert N_2 atmosphere and then resuspended in fat-free bovine serum albumin (BSA) (4 mg/ml) in 1 × phosphate-buffered saline (PBS) (pH 7.4) at 125 mM, and finally added to the cultured medium at required concentration.

Measurement of S1P and DAG—S1P and DAG were measured by using high-performance liquid chromatography mass spectrometry (LC-MS/MS) methodology as described previously at the Lipidomics Shared Resource, Hollings Cancer Center (Bielawski et al., 2006; Panneer Selvam et al., 2015). The abundance of lipids was normalized to total protein and/or inorganic phosphate (Pi).

Transfection of T Cells—Naive T cells were isolated either from WT or Sphk1$^{-/-}$ mice, and then transfected with Sphk1^{empty}, Sphk1^{WT} or Sphk1^{mutant} vector, using Amaxa™ mouse T cell nucleofetor™ kit from Lonza following manufacturers' protocol. Transfected cells were cultured either in Th0 or Treg differentiation media described in the previous section for 48 hours.

Retroviral Transduction—One day before transfection, 5×10^6 Platinum-E ecotropic packaging cells (Cell Biolabs) were seeded in 10 mL antibiotic-free medium in 100 mm dishes (Corning). Packaging cells were transfected with 18 mg retroviral plasmid DNA encoding either TIL 1383I TCR or PPARγ empty/WT/mutant vector and the helper plasmid pCL-Eco using 36 mL Lipofectamine 2000 in OptiMEM (Invitrogen). After 24hr, medium was replaced and the cells were incubated for additional 24hr, after which the retrovirus-containing supernatant was collected and filtered. The viral supernatant was spun at 2,000 g for 2 hr at 32° C onto non-tissue-culture-treated 24-well plates (USA Scientific) coated overnight with Retronectin (Takara Bio). Freshly isolated mouse $CD4^+$ T cells were activated with CD3/CD28-coated beads (Dynabeads, Life Technologies) at a 1:1 bead: cell ratio along with either T cell differentiation media (as described above) or IL2 containing media (100 U/ml) the same day as packaging cell transfection. Beads were removed 48 hr post-activation, just prior to transduction, and re-suspended to a concentration of 2×10^6 cells ml-1 in fresh medium. After removing the virus from the Retronectin-coated plate following the first spin, 1 mL of the activated T cells were then plated in the same wells and 1 mL of fresh virus was added on top of the cells. The plate was spun for an additional 2 hr at 1100 g, 32° C. Post-spin, 1 mL of media was removed and replaced with fresh media containing 200 IU/ml IL-2 before the cells were incubated overnight. The following day the cells were collected, washed, and plated at 10^6 cells/ml.

Flow Cytometry—Staining for cell surface markers was performed by incubating cells with antibody at 1:200 dilutions in FACS buffer (0.1% BSA in PBS) for 30 min at 4°C. For intracellular cytokine (IFNγ and IL17a) and Sphk1 staining, surface markers were stained before fixation/permeabilization (BD Cytofix/Cytoperm Kit, BD Biosciences, San Jose, CA). For staining of transcription factors (PPARγ, RORγT, IRF-4), cells were stained with surface markers and fixed/permeabilized with FoxP3 staining buffer set (eBioscience, San Diego, CA). For pFoxo1 staining, cells were fixed/permeabilized using BD perm III buffer set (BD Bioscience, San Jose, CA) before staining with cell surface markers and pFoxo1 primary antibody (Cell Signaling Technologies, Danvers, MA), followed by fluorochrome-conjugated secondary antibody (Jackson ImmunoResearch Laboratories, West Grove, PA). Samples were acquired on LSRFortessa and analyzed with FlowJo software (Tree Star, OR).

Real-time Quantitative PCR—Total RNA was extracted from pellets of the indicated T cell subsets (2×10^6 cells) using Trizol reagent (Life technologies, Grand Island, NY). cDNA was generated from 1 μg total RNA using iScript cDNA Synthesis Kit (BioRad, Hercules, CA). SYBR Green incorporation quantitative real-time PCR was performed using a SYBR Green mix (Biorad, Hercules, CA) in the CFX96 Detection System (BioRad, Hercules, CA). Expression of different genes was quantified relative to *Actb.*

Immunoblotting—For evaluation of the protein level of Sphk1, PPARγ and pFoxo1 live cells were sorted using FACS and then pellets were washed in PBS and lysed in RIPA buffer (25mM Tris-HCl pH: 7.4, 150mM NaCl, 1% Triton X-100, 1% sodium deoxycholate, EDTA (20ul 0f 0.5M stock) including protease/phosphatase inhibitors using a gauge (26.5%) syringe five times, incubated for 20 minutes on ice. Cell lysates were then centrifuged at 12000 g for 15 min at 4°C. The supernatant was collected and proteins were quantified with

Bradford method. For immunoblot analyses, 40 μg of protein lysates per sample were denatured in 2X Loading dye and boiled using a heating block at 95 degrees for 10 minutes before loading to SDS gradient gels 4%–20% (Bio Rad Criterion, 1h runs). Gels were semi-dry transferred onto PVDF and the membranes were blocked with 5% milk in 0.1% TBST. Membrane was probed with either anti-Sphk1 antibody (Abcam, Cambridge, MA) or anti-PPARγ (Cell Signaling Technology, Danvers, MA) pFoxo1 (Cell Signaling Technology, Danvers, MA) pAkt (Cell Signaling Technology, Danvers, MA) overnight at 4°C followed by 1 hr incubation with HRP-conjugated secondary antibody (Sigma, St. Louis, MO) and using a chemiluminescence kit (SuperSignal West Dura Extended Duration Substrate, Thermo Fisher Scientific, Waltham, MA).

For evaluation of nuclear localization of Foxo1, cells were lysed using NE-PER Nuclear and Cytoplasmic Extraction Reagents (Thermo Fisher Scientific, Waltham, MA) and nuclear fraction was isolated according to the manufacturer's protocol. Same membrane was stripped with stripping buffer (Bioland Scientific, Paramount, CA) according to manufacturer's protocol and re-probed with antibody specific to TBP and βtubulin (Cell Signaling Technologies, Danvers, MA) as reference control for nuclear and cytoplasmic fraction respectively.

Transmission Electron Microscopy (TEM)—The cells were pelletized and fixed in 2% Phosphate Buffered Glutaraldehyde for one hr. The pellets were rinsed in 0.1M Phosphate Buffered Rinse and then post fixed in 2% Aqueous Osmium Tetroxide for one hr. After rinsing in distilled water, the pellets were dehydrated through a series of graded Ethyl Alcohol; 50% ETOH for 15 min, 70% ETOH for 15 min, 95% ETOH for 15 min, and finally twice with 100% ETOH for 15 min each. The dehydrant was removed using the intermediate fluid, Propylene Oxide, one changes of 10 min each. The pellets were infiltrated with a 1:1 solution of propylene oxide and Embed 812 (Electron Microscopy Sciences, Ft. Washington, PA) for one hr. The infiltration was continued using a 1:2 solution of propylene oxide and Embed 812, overnight. The pellets were embedded in Embed812 the following day and polymerized in a 60°C oven for 48 hr. Preliminary 1/2 micron sections were cut and stained with Toluidine Blue, and examined using a light microscope. Then with the cell types identified, the 70nm thin sections are cut and stained with uranyl acetate and led citrate, and allowed to dry. The sections are viewed on the JEOL 1010 and images are taken with a Hamamatsu electron microscope camera.

Metabolism Assays—Oxygen consumption rate (OCR) and Extracellular acidification rate (ECAR) was determined using Seahorse Xfe96 analyzer (Agilent Technologies, Santa Clara, CA). Briefly, T cells (0.5×10^6/well) were plated on a Cell-Tak coated Seahorse culture plate for 30 min. OCR, a measure of OXPHOS, was analyzed under basal condition, or in response to 200 μM Etomoxir, followed by 1.0 mM oligomycin, 1.0 μM fluoro-carbonyl cyanide phenylhydrazone (FCCP) and 2 μM rotenone, plus 100 nM antimycin A. ECAR, a measure of glycolysis, was measured under basal conditions and in response to glucose (5.5 mM), Oligomycin (1.0 μM), and 2-deoxyglucose (2-DG) (100 mM). All reagents were purchased from Sigma-Aldrich, St. Louis, MO.

Measurement of ATP, TAG, and Cholesterol—ATP was measured with a commercially available kit (FLAA, Sigma) using bioluminescence at 560 nm, as described previously (Sentelle et al., 2012). TAG and cholesterol were measured using commercially available kits TR22421and TR13421 (ThermoFisher), as described in the manufacturer's protocol.

Activity Assay of PPAR Isoforms and Foxo1—Using equal amounts of nuclear protein extracted by NE-PER Nuclear and Cytoplasmic Extraction Reagents (Thermo Fisher Scientific, Waltham, MA), PPAR isoform activity (Transcription Factor PPAR 96-Well Strip Plate; Cayman chemical company) and Foxo1 activity (FKHR transcription Factor Assay Kit, Active Motif, Carlsbad, CA) were determined, as per manufacturer's protocol.

Isolation of Tumor Infiltrating T Cells—To obtain tumor-infiltrating T cells (TILs) from subcutaneously established solid B16-F10 melanoma-bearing mice, tumors were excised, chopped finely using tweezers and scissors, and then digested with 2 mg/ml collagenase type IV (Stemcell technologies, Vancouver, BC) for 45 min. Following digestion, tumors were filtered through 70μM cell strainers (BD Biosciences, San Jose, CA). The cell suspension was washed in culture medium twice by centrifugation at 1500 rpm for 10 min at 4°C. After the second wash, the cells were re-suspended in 6 mL PBS and layered carefully over 3 mL Ficoll-paque (GE healthcare) followed by centrifugation at 1500 rpm for 30 min at room temperature. The enriched TILs obtained at the interface as a thin buffy layer, were washed with PBS twice and finally re-suspended in FACS staining buffer for further staining procedures.

RNA Sequencing—The Illumina TruSeq Stranded mRNA Library Prep kit was used for library preparation (Illumina, San Diego, CA). The samples were sequenced on the Illumina HiSeq 2500 platform rendering 50 bp single-end reads. Adaptor sequences and low quality sequences were removed using Cutadapt v. 1.11. The resulting reads were mapped to GRCm38 using Tophat2 v. 2.0.13. Counts were generated using HTSeq v. 0.6.1p1 and DESeq2_1.14.1 was used to determine differential expression.

QUANTIFICATION AND STATISTICAL ANALYSIS

All data reported are the arithmetic mean from three or five independent experiments performed in triplicate ± SD unless stated otherwise. The unpaired Student's t test was used to evaluate the significance of differences observed between groups, accepting $p < 0.05$ as a threshold of significance. Data analyses were performed using the Prism software (GraphPad, San Diego, CA). Analyses of time-to-sacrifice and tumor size (mm^2) were performed using *R* statistical software version 3.2.3 and SAS version 9.4. Time-to-sacrifice was censored for animals not meeting conditions for sacrifice at the end of the experiment. Graphical displays of survival probabilities were constructed using Kaplan-Meier plots. Log-rank tests were used to compare survival probabilities between experimental groups.

Tumor growth over time was modeled using linear mixed effects regression. We used a log base 2 transformation of tumor size to achieve approximate normality. Models included fixed effects for experimental condition and time (as a continuous variable) and their two-

way interaction, and mouse-specific random effects to accommodate the correlation between measures obtained from the same animal over time. In cases where data were pooled across multiple experiments, models were appropriately adjusted for experiment effects. All models further adjusted for baseline tumor size to accommodate differences in tumor size at treatment initiation. Group comparisons at specific time points were performed using model-based linear contrasts.

Power Analysis—Methods S1 shows power to detect a survival probability of 50%, 60% or 70% versus a null survival probability of 5% at a given time point based on a log-rank test with two-sided $\alpha = 0.05$. The differences between the null and alternative survival probabilities are large, but we expect differences that translate clinically to be large in our *in vivo* models. For group sample sizes of 10, only the largest differences are detectable with approximately 80% power. However, with a group sample size of 14 animals, all differences considered are detectable with 80% power. The majority of our experiments were performed using between 10 and 14 animals per group. We therefore consider our experiments to be appropriately powered to detect clinically meaningful differences. Finally, we note that in cases where data from multiple experiments were pooled to achieve the appropriate group sample size, analyses were appropriately modified to adjust for any batch effect attributed to the experiment.

DATA AND CODE AVAILABILITY

The RNA sequencing data are published with Gene Expression Omnibus (GEO). The accession number is GEO: GSE129489.

Supplementary Material

Refer to Web version on PubMed Central for supplementary material.

ACKNOWLEDGMENTS

We thank Dr. Sarah Spiegel (Virginia Commonwealth University) for providing us with WT and mutant SphK1 plasmids. The authors sincerely acknowledge help from Mr. Brett Bechtol at HCC in preparation of this manuscript. We also acknowledge support from Ms. Nancy Smythe for electron microscopy images at MUSC. The work was supported in part by NIH, United States (R21CA137725, R01CA138930, and P01CA154778 [MUSC sub-contract] to S.M. and R01CA173687, R01CA214461, R01DE016572, and PO1 CA203628 to B.O.) and the SmartState Endowment in Lipidomics and Drug Discovery (to B.O.). The American Association of Immunologists, United States, Careers in Immunology Fellowship supported P.C. from 2018–19. We also acknowledge support from Hollings Cancer Center Shared Resources (partly supported by P30 CA138313) at MUSC.

REFERENCES

Al-Hommrani M, Chakraborty P, Chatterjee S, and Mehrotra S (2016). Dynamic Metabolism in Immune Response. J. Immunol. Res. Ther 1, 37–48. [PubMed: 27774525]

Alvarez SE, Harikumar KB, Hait NC, Allegood J, Strub GM, Kim EY, Maceyka M, Jiang H, Luo C, Kordula T, et al. (2010). Sphingosine-1-phosphate is a missing cofactor for the E3 ubiquitin ligase TRAF2. Nature 465, 1084–1088. [PubMed: 20577214]

Bachmann MF, Wolint P, Schwarz K, Jäger P, and Oxenius A (2005). Functional properties and lineage relationship of CD8+ T cell subsets identified by expression of IL-7 receptor alpha and CD62L. J. Immunol 175, 4686–4696. [PubMed: 16177116]

Bielawski J, Szulc ZM, Hannun YA, and Bielawska A (2006). Simultaneous quantitative analysis of bioactive sphingolipids by high-performance liquid chromatography-tandem mass spectrometry. Methods 39, 82–91. [PubMed: 16828308]

Bonder CS, Sun WY, Matthews T, Cassano C, Li X, Ramshaw HS, Pitson SM, Lopez AF, Coates PT, Proia RL, et al. (2009). Sphingosine kinase regulates the rate of endothelial progenitor cell differentiation. Blood 113, 2108–2117. [PubMed: 19109558]

Bonnaud S, Niaudet C, Legoux F, Corre I, Delpon G, Saulquin X, Fuks Z, Gaugler MH, Kolesnick R, and Paris F (2010). Sphingosine-1-phosphate activates the AKT pathway to protect small intestines from radiation-induced endothelial apoptosis. Cancer Res 70, 9905–9915. [PubMed: 21118968]

Bouquerel P, Gstalder C, Mu€ller D, Laurent J, Brizuela L, Sabbadini RA, Malavaud B, Pyronnet S, Martineau Y, Ader I, and Cuvillier O (2016). Essential role for SphK1/S1P signaling to regulate hypoxia-inducible factor 2a expression and activity in cancer. Oncogenesis 5, e209. [PubMed: 26974204]

Buck MD, O'Sullivan D, and Pearce EL (2015). T cell metabolism drives immunity. J. Exp. Med 212, 1345–1360. [PubMed: 26261266]

Chakrabarti P, English T, Karki S, Qiang L, Tao R, Kim J, Luo Z, Farmer SR, and Kandror KV (2011). SIRT1 controls lipolysis in adipocytes via FOXO1-mediated expression of ATGL. J. Lipid Res 52, 1693–1701. [PubMed: 21743036]

Chang CH, Qiu J, O'Sullivan D, Buck MD, Noguchi T, Curtis JD, Chen Q, Gindin M, Gubin MM, van der Windt GJ, et al. (2015). Metabolic Competition in the Tumor Microenvironment Is a Driver of Cancer Progression. Cell 162, 1229–1241. [PubMed: 26321679]

Chatterjee S, Daenthanasanmak A, Chakraborty P, Wyatt MW, Dhar P, Selvam SP, Fu J, Zhang J, Nguyen H, Kang I, et al. (2018). CD38-NAD(+) Axis Regulates Immunotherapeutic Anti-Tumor T Cell Response. Cell Metab 27, 85–100. [PubMed: 29129787]

Chi H (2011). Sphingosine-1-phosphate and immune regulation: trafficking and beyond. Trends Pharmacol. Sci 32, 16–24. [PubMed: 21159389]

Clark RB, Bishop-Bailey D, Estrada-Hernandez T, Hla T, Puddington L, and Padula SJ (2000). The nuclear receptor PPAR gamma and immunoregulation: PPAR gamma mediates inhibition of helper T cell responses. J. Immunol 164, 1364–1371. [PubMed: 10640751]

Fan W, Imamura T, Sonoda N, Sears DD, Patsouris D, Kim JJ, and Olefsky JM (2009). FOXO1 transrepresses peroxisome proliferator-activated receptor gamma transactivation, coordinating an insulin-induced feed-forward response in adipocytes. J. Biol. Chem 284, 12188–12197. [PubMed: 19246449]

Gattinoni L, Klebanoff CA, and Restifo NP (2012). Paths to stemness: building the ultimate antitumour T cell. Nat. Rev. Cancer 12, 671–684. [PubMed: 22996603]

Gubbels Bupp MR, Edwards B, Guo C, Wei D, Chen G, Wong B, Masteller E, and Peng SL (2009). T cells require Foxo1 to populate the peripheral lymphoid organs. Eur. J. Immunol 39, 2991–2999. [PubMed: 19658095]

Hait NC, Sarkar S, Le Stunff H, Mikami A, Maceyka M, Milstien S, and Spiegel S (2005). Role of sphingosine kinase 2 in cell migration toward epidermal growth factor. J. Biol. Chem 280, 29462–29469. [PubMed: 15951439]

Hait NC, Allegood J, Maceyka M, Strub GM, Harikumar KB, Singh SK, Luo C, Marmorstein R, Kordula T, Milstien S, and Spiegel S (2009). Regulation of histone acetylation in the nucleus by sphingosine-1-phosphate. Science 325, 1254–1257. [PubMed: 19729656]

Hess Michelini R, Doedens AL, Goldrath AW, and Hedrick SM (2013). Differentiation of CD8 memory T cells depends on Foxo1. J. Exp. Med 210, 1189–1200. [PubMed: 23712431]

Howie D, Ten Bokum A, Necula AS, Cobbold SP, and Waldmann H (2018). The Role of Lipid Metabolism in T Lymphocyte Differentiation and Survival. Front. Immunol 8, 1949. [PubMed: 29375572]

Hsu CK, Lin CC, Hsiao LD, and Yang CM (2015). Mevastatin ameliorates sphingosine 1-phosphate-induced COX-2/PGE2-dependent cell migration via FoxO1 and CREB phosphorylation and translocation. Br. J. Pharmacol 172, 5360–5376. [PubMed: 26359950]

Jones DC, Manning BM, and Daynes RA (2002). A role for the peroxisome proliferator-activated receptor alpha in T-cell physiology and ageing immunobiology. Proc. Nutr. Soc 61, 363–369. [PubMed: 12296295]

Kaur N, Naga OS, Norell H, Al-Khami AA, Scheffel MJ, Chakraborty NG, Voelkel-Johnson C, Mukherji B, and Mehrotra S (2011). T cells expanded in presence of IL-15 exhibit increased antioxidant capacity and innate effector molecules. Cytokine 55, 307–317. [PubMed: 21602054]

Kim JH, Song J, and Park KW (2015). The multifaceted factor peroxisome proliferator-activated receptor g (PPARγ) in metabolism, immunity, and cancer. Arch. Pharm. Res 38, 302–312. [PubMed: 25579849]

Klotz L, Burgdorf S, Dani I, Saijo K, Flossdorf J, Hucke S, Alferink J, Nowak N, Beyer M, Mayer G, et al. (2009). The nuclear receptor PPAR gamma selectively inhibits Th17 differentiation in a T cell-intrinsic fashion and suppresses CNS autoimmunity. J. Exp. Med 206, 2079–2089. [PubMed: 19737866]

Lee CH, and Evans RM (2002). Peroxisome proliferator-activated receptor-gamma in macrophage lipid homeostasis. Trends Endocrinol. Metab 13, 331–335. [PubMed: 12217489]

Lettieri Barbato D, Tatulli G, Aquilano K, and Ciriolo MR (2013). FoxO1 controls lysosomal acid lipase in adipocytes: implication of lipophagy during nutrient restriction and metformin treatment. Cell Death Dis 4, e861. [PubMed: 24136225]

Liu G, Yang K, Burns S, Shrestha S, and Chi H (2010). The S1P(1)-mTOR axis directs the reciprocal differentiation of T(H)1 and T(reg) cells. Nat. Immunol 11, 1047–1056. [PubMed: 20852647]

Matloubian M, Lo CG, Cinamon G, Lesneski MJ, Xu Y, Brinkmann V, Allende ML, Proia RL, and Cyster JG (2004). Lymphocyte egress from thymus and peripheral lymphoid organs is dependent on S1P receptor 1. Nature 427, 355–360. [PubMed: 14737169]

Newton R, Priyadharshini B, and Turka LA (2016). Immunometabolism of regulatory T cells. Nat. Immunol 17, 618–625. [PubMed: 27196520]

O'Sullivan D, van der Windt GJ, Huang SC, Curtis JD, Chang CH, Buck MD, Qiu J, Smith AM, Lam WY, DiPlato LM, et al. (2014). Memory CD8(+) T cells use cell-intrinsic lipolysis to support the metabolic programming necessary for development. Immunity 41, 75–88. [PubMed: 25001241]

Ogretmen B (2018). Sphingolipid metabolism in cancer signalling and therapy. Nat. Rev. Cancer 18, 33–50. [PubMed: 29147025]

Panigrahy D, Singer S, Shen LQ, Butterfield CE, Freedman DA, Chen EJ, Moses MA, Kilroy S, Duensing S, Fletcher C, et al. (2002). PPARgamma ligands inhibit primary tumor growth and metastasis by inhibiting angiogenesis. J. Clin. Invest 110, 923–932. [PubMed: 12370270]

Panneer Selvam S, De Palma RM, Oaks JJ, Oleinik N, Peterson YK, Stahelin RV, Skordalakes E, Ponnusamy S, Garrett-Mayer E, Smith CD, and Ogretmen B (2015). Binding of the sphingolipid S1P to hTERT stabilizes telomerase at the nuclear periphery by allosterically mimicking protein phosphorylation. Sci. Signal 8, ra58. [PubMed: 26082434]

Parham KA, Zebol JR, Tooley KL, Sun WY, Moldenhauer LM, Cockshell MP, Gliddon BL, Moretti PA, Tigyi G, Pitson SM, and Bonder CS (2015). Sphingosine 1-phosphate is a ligand for peroxisome proliferator-activated receptor-g that regulates neoangiogenesis. FASEB J 29, 3638–3653. [PubMed: 25985799]

Picard F, Kurtev M, Chung N, Topark-Ngarm A, Senawong T, Machado De Oliveira R, Leid M, McBurney MW, and Guarente L (2004). Sirt1 promotes fat mobilization in white adipocytes by repressing PPAR-gamma. Nature 429, 771–776. [PubMed: 15175761]

Ponnusamy S, Selvam SP, Mehrotra S, Kawamori T, Snider AJ, Obeid LM, Shao Y, Sabbadini R, and Ogretmen B (2012). Communication between host organism and cancer cells is transduced by systemic sphingosine kinase 1/sphingosine 1-phosphate signalling to regulate tumour metastasis. EMBO Mol. Med 4, 761–775. [PubMed: 22707406]

Qu P, Du H, Wilkes DS, and Yan C (2009). Critical roles of lysosomal acid lipase in T cell development and function. Am. J. Pathol 174, 944–956. [PubMed: 19179613]

Rosenberg SA, and Restifo NP (2015). Adoptive cell transfer as personalized immunotherapy for human cancer. Science 348, 62–68. [PubMed: 25838374]

Saddoughi SA, Song P, and Ogretmen B (2008). Roles of bioactive sphingolipids in cancer biology and therapeutics. Subcell. Biochem 49, 413–440. [PubMed: 18751921]

Schnute ME, McReynolds MD, Kasten T, Yates M, Jerome G, Rains JW, Hall T, Chrencik J, Kraus M, Cronin CN, et al. (2012). Modulation of cellular S1P levels with a novel, potent and specific inhibitor of sphingosine kinase-1. Biochem. J 444, 79–88. [PubMed: 22397330]

Seargent JM, Yates EA, and Gill JH (2004). GW9662, a potent antagonist of PPARgamma, inhibits growth of breast tumour cells and promotes the anti-cancer effects of the PPARgamma agonist rosiglitazone, independently of PPARgamma activation. Br. J. Pharmacol 143, 933–937. [PubMed: 15533890]

Sentelle RD, Senkal CE, Jiang W, Ponnusamy S, Gencer S, Selvam SP, Ramshesh VK, Peterson YK, Lemasters JJ, Szulc ZM, et al. (2012). Ceramide targets autophagosomes to mitochondria and induces lethal mitophagy. Nat. Chem. Biol 8, 831–838. [PubMed: 22922758]

Stayrook KR, Mack JK, Cerabona D, Edwards DF, Bui HH, Niewolna M, Fournier PG, Mohammad KS, Waning DL, and Guise TA (2015). TGFβ-Mediated induction of SphK1 as a potential determinant in human MDA-MB-231 breast cancer cell bone metastasis. Bonekey Rep 4, 719. [PubMed: 26157579]

Stephens FB, Constantin-Teodosiu D, and Greenhaff PL (2007). New insights concerning the role of carnitine in the regulation of fuel metabolism in skeletal muscle. J. Physiol 581, 431–444. [PubMed: 17331998]

Tamori Y, Masugi J, Nishino N, and Kasuga M (2002). Role of peroxisome proliferator-activated receptor-gamma in maintenance of the characteristics of mature 3T3-L1 adipocytes. Diabetes 51, 2045–2055. [PubMed: 12086932]

Van Brocklyn JR, and Williams JB (2012). The control of the balance between ceramide and sphingosine-1-phosphate by sphingosine kinase: oxidative stress and the seesaw of cell survival and death. Comp. Biochem. Physiol. B Biochem. Mol. Biol 163, 26–36. [PubMed: 22613819]

van der Windt GJ, Everts B, Chang CH, Curtis JD, Freitas TC, Amiel E, Pearce EJ, and Pearce EL (2012). Mitochondrial respiratory capacity is a critical regulator of CD8+ T cell memory development. Immunity 36, 68–78. [PubMed: 22206904]

Wei S, Zhao E, Kryczek I, and Zou W (2012). Th17 cells have stem cell-like features and promote long-term immunity. OncoImmunology 1, 516–519. [PubMed: 22754771]

Wohlfert EA, Nichols FC, Nevius E, and Clark RB (2007). Peroxisome proliferator-activated receptor gamma (PPARgamma) and immunoregulation: enhancement of regulatory T cells through PPARgamma-dependent and -independent mechanisms. J. Immunol 178, 4129–4135. [PubMed: 17371968]

Xu Y, Dong B, Wang J, Zhang J, Xue W, and Huang Y (2018). Sphingosine kinase 1 overexpression contributes to sunitinib resistance in clear cell renal cell carcinoma. OncoImmunology 7, e1502130. [PubMed: 30524898]

Yamanaka M, Shegogue D, Pei H, Bu S, Bielawska A, Bielawski J, Pettus B, Hannun YA, Obeid L, and Trojanowska M (2004). Sphingosine kinase 1 (SPHK1) is induced by transforming growth factor-beta and mediates TIMP-1 up-regulation. J. Biol. Chem 279, 53994–54001. [PubMed: 15485866]

Yang L, Pang Y, and Moses HL (2010). TGF-beta and immune cells: an important regulatory axis in the tumor microenvironment and progression. Trends Immunol 31, 220–227. [PubMed: 20538542]

Zamora-Pineda J, Kumar A, Suh JH, Zhang M, and Saba JD (2016). Dendritic cell sphingosine-1-phosphate lyase regulates thymic egress. J. Exp. Med 213, 2773–2791. [PubMed: 27810923]

Zhang MA, Rego D, Moshkova M, Kebir H, Chruscinski A, Nguyen H, Akkermann R, Stanczyk FZ, Prat A, Steinman L, and Dunn SE (2012). Peroxisome proliferator-activated receptor (PPAR)a and -γ regulate IFNγ and IL-17A production by human T cells in a sex-specific way. Proc. Natl. Acad. Sci. USA 109, 9505–9510. [PubMed: 22647601]

Highlights

- S1PR-independent intrinsic S1P signaling activates PPARγ to skew the Treg/Th17 balance
- S1P-PPARγ activation inversely correlates with lipolysis and regulates Tcm phenotype
- Inhibiting SphK1/S1P/PPARγ signaling improves T cell-mediated tumor control

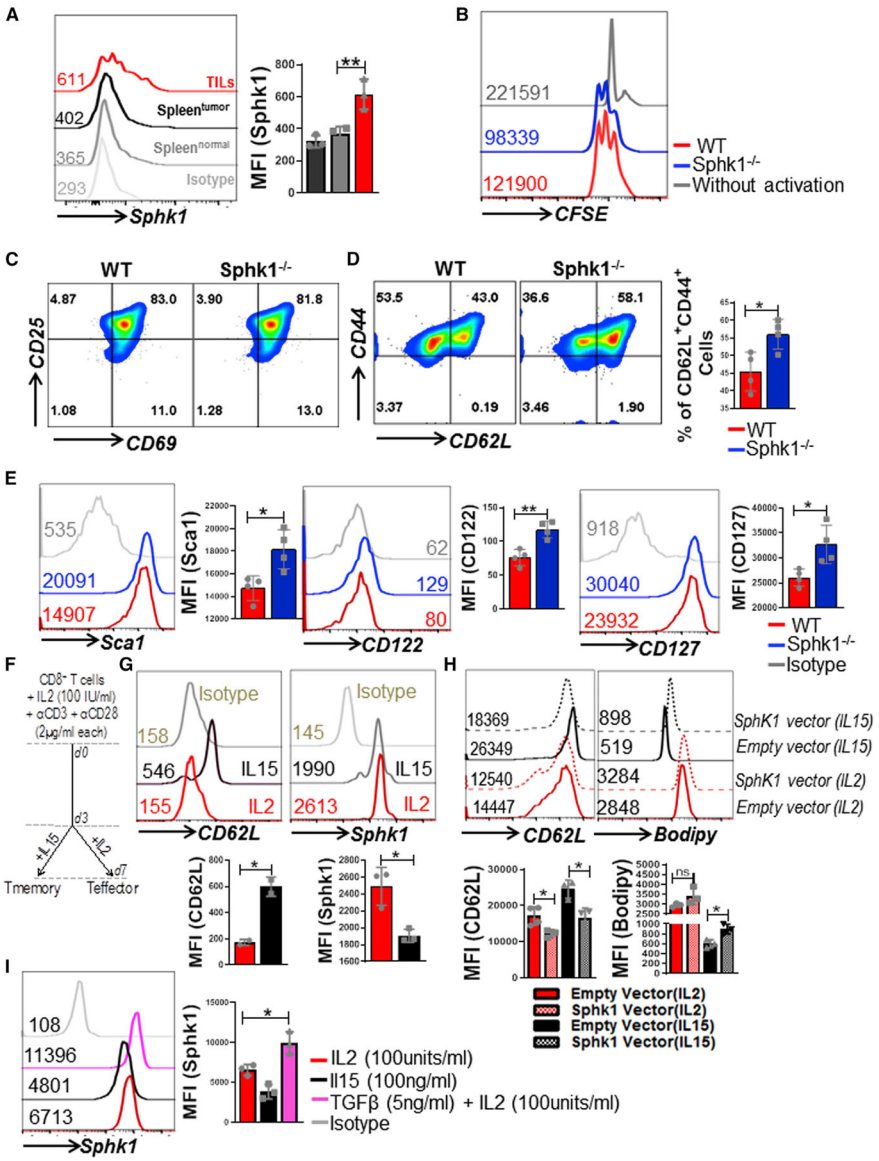

Figure 1. Activated *SphK1*$^{-/-}$ T Cells Preserve Tcm Phenotype

(A) Tumor infiltrating lymphocytes (TILs) and splenocytes were isolated from healthy or B16-F10 murine melanoma bearing C57BL/6 mice, and flow cytometry-based determination of intracellular SphK1 levels in CD8^{+} T cells was performed.

(B) CFSE dilution was analyzed by flow cytometry to determine the antigen-specific proliferation in activated pMel and *pMel-SphK*$^{-/-}$ T cells.

(C–E) Antigen-activated pMel and *pMel-SphK*$^{-/-}$ splenic T cells were used for determining the flow cytometry-based cell surface expression of (C) CD25 and CD69, (D) CD62L and CD44, and (E) Sca1, CD127, and CD122.

(F) Schematic diagram showing the strategy to generate memory T cells *in vitro* that were used for data in (G).

(G) Cells obtained using strategy in (F) with different cytokines post day 3 (IL-2 at 100 IU/mL, and IL-15 at 100 ng/mL, respectively) were analyzed for determining the flow cytometry-based cell surface expression of CD62L and intracellular expression of SphK1.
(H) Day 3 TCR-activated WT T cells were transfected with either WT vector or empty vector for SphK1 enzyme. Cells were subsequently cultured for another 3 days, either in presence of IL-2 (100 IU/mL), or IL-15 (100 ng/mL). After 3 days, expression of CD62L and SphK1 was evaluated in $CD8^+$ T cells by flow cytometry.
(I) Day 3 TCR-activated WT T cells were further cultured for 3 days, either in presence of IL-2 (100 IU/mL) or in presence of TGF-β (5 ng/mL) and IL-2 (100 IU/mL). Cells were then used to determine the intracellular expression of SphK1. Data were analyzed using FlowJo software. The numerical values within the fluorescence-activated cell sorting (FACS) overlay plots indicate MFI, and the adjacent bar diagrams represent cumulative data from at least three repeat experiments. Error bars represent mean ± SD; *$p < 0.05$.
See also Figure S1.

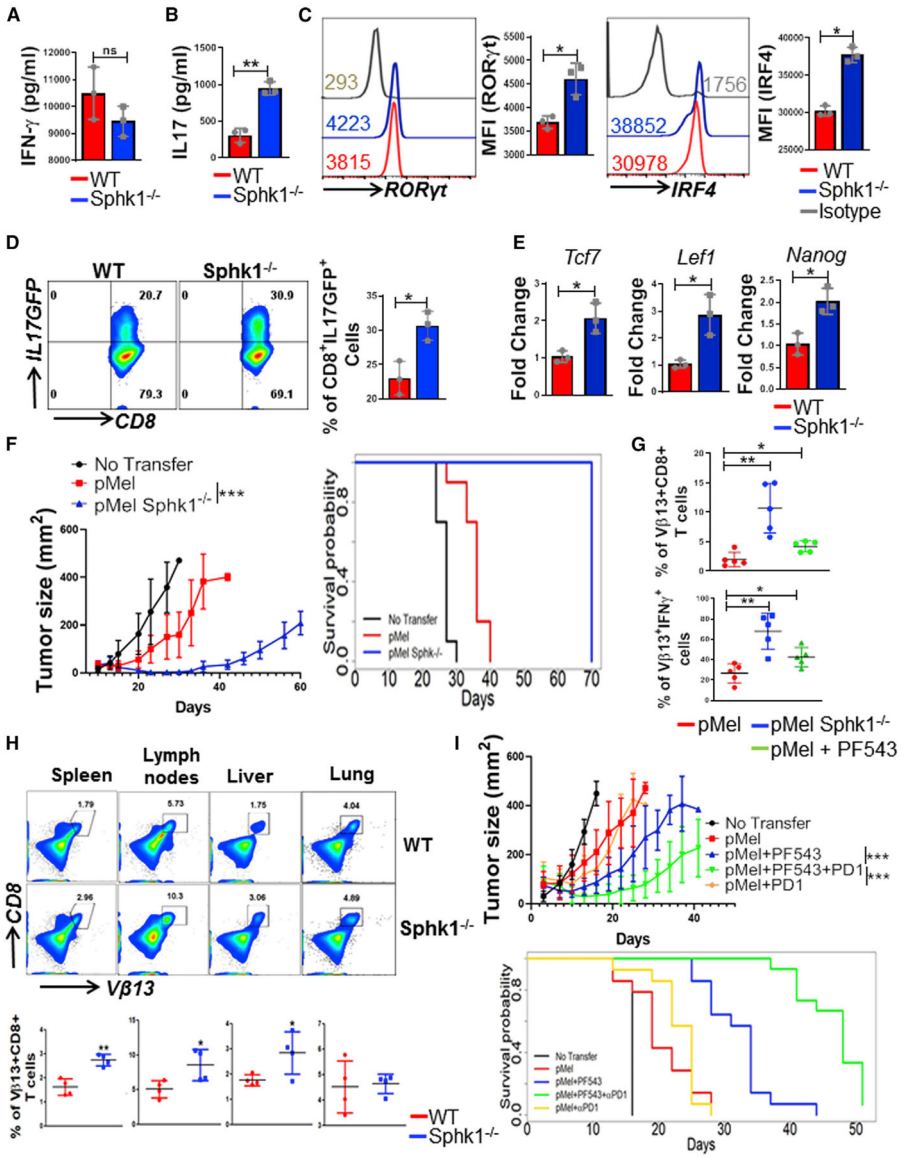

Figure 2. *SphK1*$^{-/-}$ T Cells Secrete Both IFN-γ and IL-17 upon TCR Stimulation

(A–C) pMel and *pMel-SphK*$^{-/-}$ T cells activated for 3 days with cognate antigen gp100 were antigen-restimulated overnight, and the supernatant was used for ELISA-based determination of secreted cytokine: (A) IFN-γ, (B) IL-17, (C) RORγt and IRF4 levels.

(D) Splenic T cells from IL-17-GFP reporter or *SphK1*$^{-/-}$-IL-17-GFP mice were cultured in Th17 polarizing condition for 3 days, restimulated with anti-CD3 (2 μg/mL) and anti-CD28 antibody (5 μg/mL) for 4 h, and the percentage of IL-17-GFP-positive cells were determined by flow cytometry.

(E) Three-day TCR-activated WT and *SphK1*$^{-/-}$ T cells were analyzed for expression of stemness-associated genes using mRNA. Data are representative of three independent experiments in (A)–(E).

(F) C57BL/6 mice (n = 10 mice/group) were inoculated subcutaneously (s.c.) with 0.3 × 10^6 B16-F10 melanoma cells for 9 days, after which mice were either kept untreated or

adoptively transferred, either with 1×10^6 pMel or *pMel-SphK1*$^{-/-}$ T cells. Tumor growth was measured using digital calipers twice weekly. Left panel: estimated growth curves for each experimental condition. Right panel: survival curve (p value pMel versus pMel *SphK1*$^{-/-}$ is 1e–05).

(G) Upper panel: C57BL/6 mice (n = 5 mice/group) were inoculated (s.c.) with 0.25×10^6 B16-F10 melanoma cells for 14 days, then 1×10^6 3 days gp100-activated pMel T cells, pMel *SphK1*$^{-/-}$ T cells, or pMel T cells treated with PF543 (1 μM) were adoptively transferred. After 15 days, lymphocytes were retrieved from the excised tumor to determine the percentage of TCR transgenic T cell. Lower panel: retrieved lymphocytes (as in upper panel) were stimulated overnight with gp100 peptide antigen before staining with fluorochrome-conjugated antibodies to determine intracellular IFN-γ levels.

(H) Upper panel: representative flow cytometric analysis of donor cells retrieved from the lung, liver, spleen, and lymph nodes 48 h after adoptive transfer of pMel or *pMel-SphK*$^{-/-}$ T cells into *Rag1*$^{-/-}$ mice (n = 3). Lower panel: composite data from different mice.

(I) C57BL/6 mice (n = 10–15/group) were inoculated (s.c.) with 0.3×10^6 B16-F10 melanoma cells for 9 days before injecting cyclophosphamide (CTX). After 24 h of CTX injection, tumor-bearing C57BL/6 were either kept untreated or adoptively transferred with 1×10^6 3 days gp100-activated pMel T cells, or pMel T cells treated with PF543 (1 μM). In the indicated groups, following ACT, recipient mice were injected intraperitoneally (i.p.) either with PF543 or anti-PD1 Ab (200 μg/mouse), or both PF543 and anti-PD1 Ab. Both PF543 and anti-PD1 Ab were given three times in a week. Upper panel: tumor growth measured using digital calipers. Lower panel: survival curve. Error bars represent mean ± SD in (A)–(I). *p < 0.05, **p < 0.01, ***p < 0.001.

See also Figure S2.

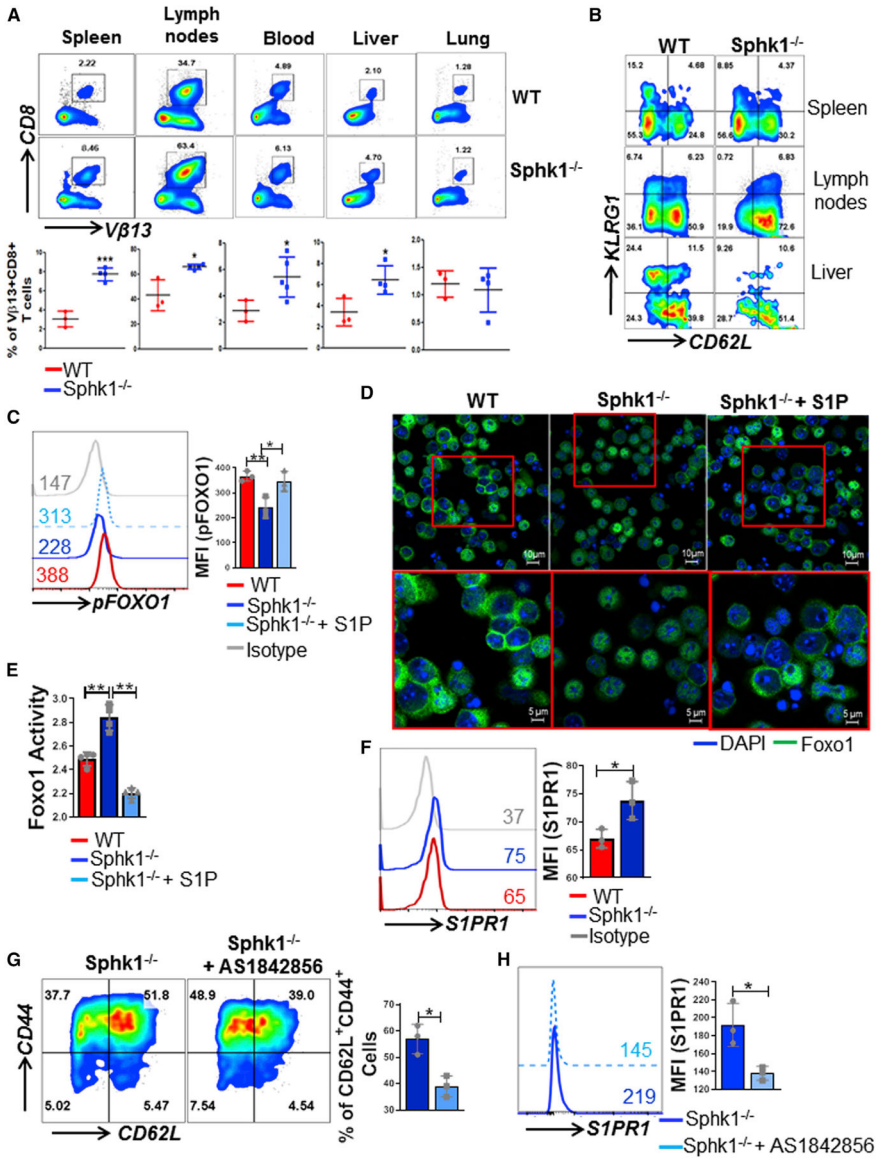

Figure 3. *SphK1*$^{-/-}$ T Cells Exhibit Improved Migration and Foxo1 Activity

(A) Three day-activated pMel or *pMel-SphK1*$^{-/-}$ T cells were adoptively transferred into *Rag1*$^{-/-}$ mice (n = 3). 25 days of post-transfer B16-F10 cells were s.c. injected. Upper panel: representative flow cytometric analysis done to determine the percentage of TCR transgenic T cells retrieved from spleen, lymph nodes, blood, liver, and lung after 5 days of tumor injection. Lower panel: cumulative data from different mice.

(B) *C*ell surface expression of KLRG1 and CD62L was determined on the retrieved cells from (A).

(C) Flow cytometry analysis of phosphorylated Foxo1 (S256) in WT, *SphK1*$^{-/-}$, and *SphK1*$^{-/-}$ T cells treated with S1P (5μM) after 3 days of TCR activation.

(D) Confocal images of the indicated cell stained with Foxo1 (in green) and nuclei stained with DAPI (in blue). Lower panels: magnified images (red boxes) of the upper panels. Scale bars represent 10 μm in upper panels and 5 μm in lower panels.

(E) Foxo1 activity in WT, *SphK1*$^{-/-}$, and *SphK1*$^{-/-}$ cells T cells treated with S1P (5 μM) in 3 days TCR-activated T cells, determined using the commercially available kit as per vendor's protocol.

(F) Flow cytometry analysis of S1PR1 on 3 days TCR-activated WT and *SphK1*$^{-/-}$ T cells.

(G and H) *SphK1*$^{-/-}$ T cells were activated in presence of AS1842856 and cell surface expression of CD62L/CD44 (G), and S1PR1 was determined using flow cytometry (H). The numerical values within the FACS overlay plots indicate MFI, and the adjacent bar diagrams represent cumulative data from multiple repeat experiments. Data are representative of at least three independent experiments and error bars represent mean ± SD in (B)–(H). *$p < 0.05$, **$p < 0.01$.

See also Figure S3.

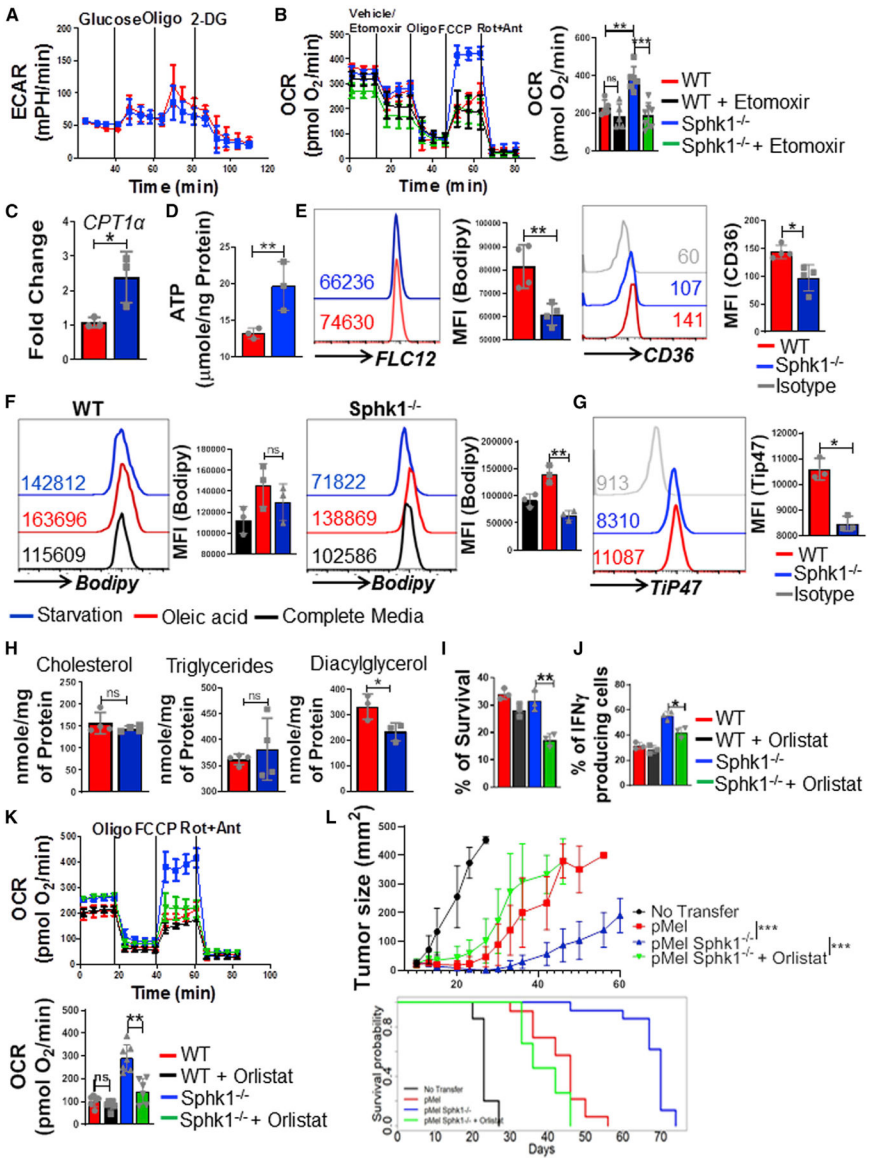

Figure 4. *SphK1*$^{-/-}$ T Cells Preferentially Depend on Oxidative Phosphorylation and Lipolysis for Energy Need

(A) Three days TCR activated WT and *SphK*$^{-/-}$ T cells were used to determine ECAR time course in response to glucose, oligomycin, and 2DG.

(B) OCR in presence or absence of etomoxir (200 μM) followed by the addition of various mitochondrial inhibitors as indicated in the figure. Graph on left represents time course, and bar diagram on right represents basal OCR values. 0.5 × 10^6 cells/well were used to perform the study.

(C) mRNA from 3 days TCR-activated WT and *SphK1*$^{-/-}$ T cells were used to determine the expression of *CPT1a* using qPCR.

(D and E) Three days activated WT and *SphK1*$^{-/-}$ T cells were used for (D) determining ATP levels and (E) Bodipy-conjugated FL C_{12} uptake (left panel), and cell surface expression of CD36 (right panel) by flow cytometry.

(F) Three days TCR activated WT and *SphK1*$^{-/-}$ T cells were cultured overnight ± oleate (30 μM), followed by 24 h of starvation in low glucose (2 mM) media and then stained with Bodipy.

(G) Activated WT and *SphK1*$^{-/-}$ T cells were used to determine the Tip47 expression by flow cytometry.

(H) Activated WT and *SphK1*$^{-/-}$ T cells were used to determine the abundance of lipid signature molecules by mass spectroscopy.

(I) WT and *SphK1*$^{-/-}$ T cells were activated either in presence or absence orlistat (100 μM), and cell viability was determined using 7AAD staining.

(J) Cells in (I) were also used for determining IFN-γ secretion by intracellular cytokine staining using flow cytometry.

(K) OCR was measured using real-time flux analysis using Seahorse and with mitochondrial inhibitors. 0.4×10^6 cells/well were used to perform the study. The numerical values within the FACS overlay plots indicate MFI, and the bar diagrams represent cumulative data from at least three repeat experiments in (A)–(K).

(L) C57/BL6 mice (n = 15 mice/group) were inoculated (s.c.) with 0.3×10^6 B16-F10 melanoma cells for 9 days, after which mice either kept untreated or adoptively transferred with 1×10^6 pMel and *pMel-SphK*$^{-/-}$ T cells cultured in presence or absence of orlistat (100 μM). Tumor growth was measured using digital calipers twice weekly. Upper panel: growth curves for each experimental condition. Lower panel: survival curve (p value; pMel versus pMel *SphK1*$^{-/-}$: 2e–06, pMel *SphK1*$^{-/-}$ + Orlistat versus pMel *SphK1*$^{-/-}$: 5e–07). *p < 0.05, **p < 0.01, ***p < 0.001. Error bars represent mean ± SD.

See also Figure S4.

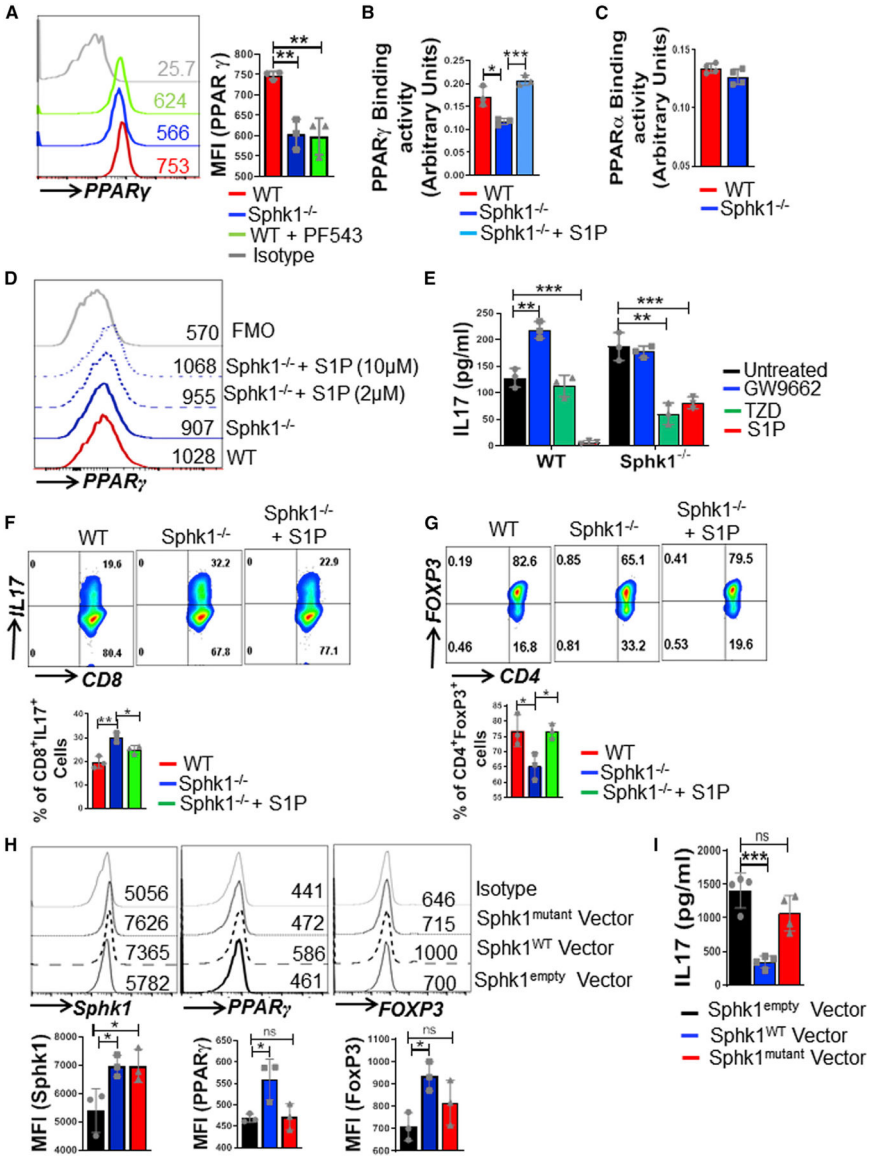

Figure 5. Reduced PPARγ Regulates Functionality and Metabolic Commitment of *SphK1*$^{-/-}$ T Cells

(A) WT and *SphK1*$^{-/-}$ T cells were activated for 3 days either in presence or absence of PF543 (1 μM) and used to determine the expression of PPARγ using flow cytometry.

(B and C) Purified T cells from WT and *SphK1*$^{-/-}$ mice were TCR activated for 3 days in presence or absence of S1P (5 μM). These T cells were used in ELISA-based assay to determine the activity of PPARγ (B) and PPARa (C).

(D) WT and *SphK1*$^{-/-}$ T cells activated for 3 days in presence or absence of indicated amount of S1P were used to determine PPARγ expression using flow cytometry.

(E) WT and *SphK1*$^{-/-}$ T cells were stimulated for 3 days in presence or absence of GW9662, TZD, or with S1P. After 3 days of stimulation, supernatant collected after overnight restimulation was used to measure IL-17 secretion by ELISA.

(F and G) WT and *SphK1*$^{-/-}$ T cells were differentiated under Th17 or Treg polarizing condition for 3 days in either the presence or absence of S1P. The percentage of IL-17-producing cells (F) and FOXP3-expressing T cells were determined (G).

(H) *SphK1*$^{-/-}$ T cells were transfected with either WT or mutant vector for SphK1 enzyme. Expression of SphK1, PPARγ, and FOXP3 was analyzed by flow cytometry.

(I) Cells in (H) were used for measuring IL-17 secretion by ELISA. *$p < 0.05$, **$p < 0.01$, ***$p < 0.001$. The numerical values within the FACS overlay plots indicate MFI. Adjacent bar diagrams represent cumulative data from at least three repeat experiments. Error bars represent mean ± SD.

See also Figure S5 and Data S1.

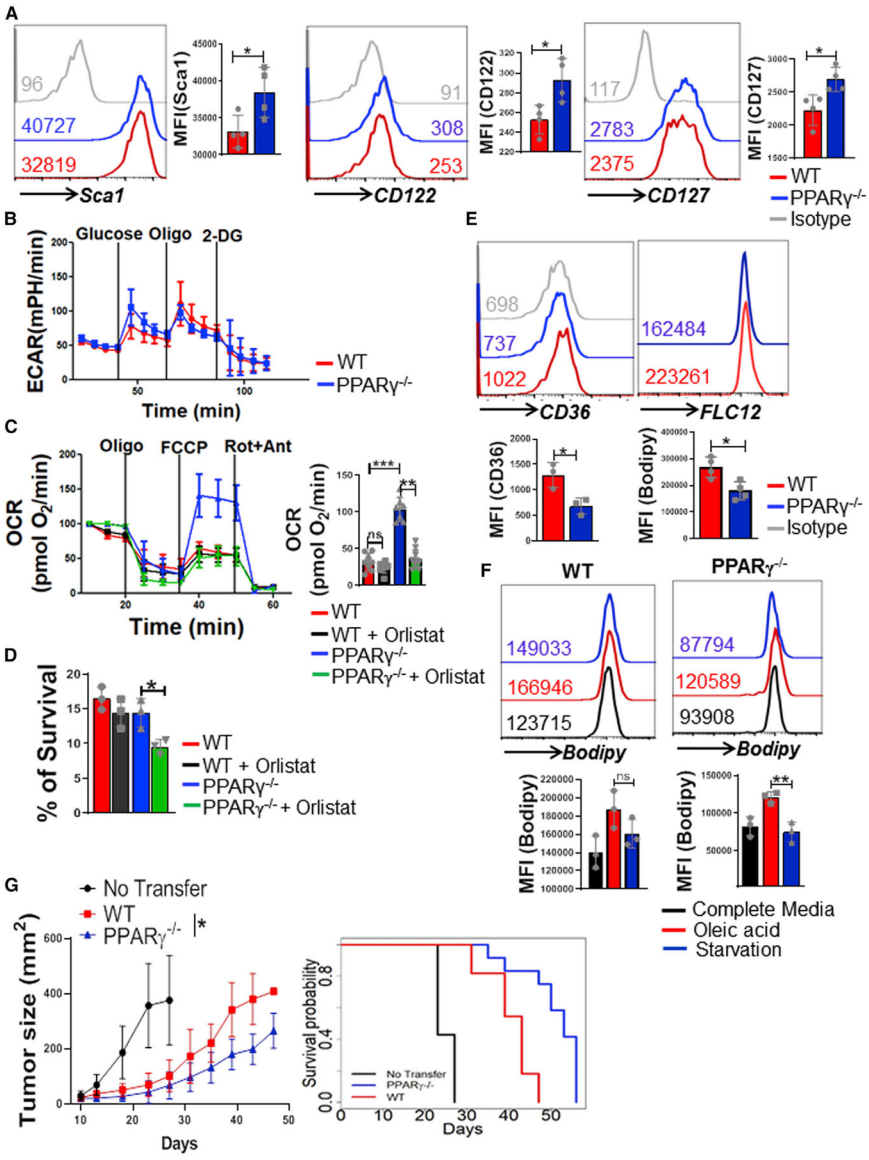

Figure 6. PPARγ-Deficient T Cells Show Improved Antitumor Potential

(A–C) Three-day activated WT and PPARγ-deficient T cells were used to determine (A) cell surface expression of stem cell antigen (Sca1), CD122, and CD127; (B) ECAR time course in response to glucose, oligomycin, and 2DG; and (C) WT and *PPARγ*$^{-/-}$ T cells were activated either in presence or absence orlistat (100 μM). OCR under basal condition and in response to indicated mitochondrial inhibitors was determined.

(D) WT and *PPARγ*$^{-/-}$ T cells were activated either in presence or absence of orlistat (100 μM) and used to determine cell viability with 7AAD staining.

(E) Bodipy conjugated FL C_{12} uptake; and expression of CD36 by flow cytometry in day 3 activated WT and *PPARγ*$^{-/-}$ T cells.

(F) Day 3 activated WT and PPARγ-deficient T cells were cultured overnight ± oleate (30 μM), followed by 24 h of starvation in low glucose (2 mM) media, and then stained with

Bodipy. The numerical values within the FACS overlay plots indicate MFI. Adjacent bar diagrams represent cumulative data from at least three repeat experiments.
(G) C57BL/6 HLA-A2^{+} mice (n = 12 mice/group) were inoculated (s.c.) with 0.3 × 10^{6} B16F10-A2^{+} melanoma cells for 9 days, after which mice either kept untreated or adoptively transferred with melanoma reactive 1 × 10^{6} TIL1383I tyrosinase epitope-reactive TCR transduced T cells generated using splenocytes from WT or *PPARγ*^{cre}*CD4*^{flox} mice. Tumor growth was measured using digital calipers twice weekly. Left: estimated growth curves for each experimental condition. Right: survival curve (p value WT versus *PPARγ*$^{-/-}$: 2e–04).
(A–G) Error bars represent mean ± SD. *p < 0.05, **p < 0.01.
See also Figure S6.

KEY RESOURCES TABLE

REAGENT or RESOURCE	SOURCE	IDENTIFIER
Antibodies		
Anti-mouse CD3	BioXCell	Clone: 145–2C11; Cat# BE0001–1; RRID: AB_1107634
Anti-mouse CD28	BioXCell	Clone: 37.51; Cat# BE0015–1; RRID: AB_1107624
Anti-mouse IL4	BioXCell	Clone: 11B11; Cat# BE0045; RRID: AB_1107707
Anti-mouse IFNγ	BioXCell	Clone: XMG1.2; Cat# BE0055; RRID: AB_1107694
CD4-PE	eBioscience	Clone: GK5.1; Cat# 12–0041-83; RRID: AB_465506
RORγ-APC	eBioscience	Clone: AFKJS-9; Cat# 17–6988-80; RRID: AB_10609207
FOXP3 -PE	eBioscience	Clone: FJK-16 s; Cat# 12–5773-82; RRID: RRID:AB_465936
IRF-4-eFluor 660	eBioscience	Clone: 3E4; Cat# 50–9858-80; RRID: AB_2574393
CXCR3-PE	eBioscience	Clone: CXCR3–173; Cat# 12–1831-80; RRID: AB_1210734
CD45.2-PE	eBioscience	Clone: 104; Cat# 12–0454-81; RRID: AB_465678
CD90.1-APC	eBioscience	Clone: HIS51; Cat# 17–0900-82; RRID: AB_1272252
CD90.1-Pacific Blue	eBioscience	Clone: HIS51; Cat# 48–0900-80; RRID: AB_1272254
CD4-PE/Cy7	Biolegend	Clone: GK5.1; Cat# 100422; RRID: AB_312707
CD4-APC	Biolegend	Clone: GK5.1; Cat# 100412; RRID: AB_312697
CD4-APC/Cy7	Biolegend	Clone: GK5.1; Cat# 100414; RRID: AB_312699
CD8-PE/Cy7	Biolegend	Clone: 53–6.7; Cat# 100722; RRID: AB_312761
CD8-APC	Biolegend	Clone: 53–6.7; Cat# 100712; RRID: AB_312751
CD8-FITC	Biolegend	Clone: 53–6.7; Cat# 100706; RRID: AB_312745
IL17-PE	Biolegend	Clone: TC11–18H10.1; Cat# 506904; RRID: AB_315464
IL17-Pacific Blue	Biolegend	Clone: TC11–18H10.1; Cat# 506918; RRID: AB_893544
IFNγ-PE	Biolegend	Clone: XMG1.2; Cat# 505808; RRID: AB_315402
IFNγ-Alexa647	Biolegend	Clone: XMG1.2; Cat# 505814; RRID: AB_493314
CCR7-PE	Biolegend	Clone: 4B12; Cat# 120105; RRID: AB_389357
CD36-APC	Biolegend	Clone: HM36; Cat# 102612; RRID:AB_2072639
CD62L-APC	Biolegend	Clone: MEL14; Cat# 104412; RRID AB_313099
CD44-PerCP/cye5.5	Biolegend	Clone: IM7; Cat# 103032; RRID AB_2076204
CD45.1-APC	BD Biosciences	Clone: A20; Cat# 558701; RRID: AB_1645214
Vβ13-FITC	BD Biosciences	Clone: MR1 2–3; Cat# 553204; RRID: AB_394706
KLRG1-PerCP/Cye5.5	BD Biosciences	Clone: 2F1; Cat# 563595
Mouse S1P1 /EDG-1 PE	R&D System	Clone: # 713412; Catalog# FAB7089P
Mouse TGF-beta RII FlTC	R&D System	Clone: # Ile24Asp184 Accession # Q62312; Catalog# FAB532F
Mouse anti-Akt (pS473) PE	BD Biosciences	Clone # M89–61 Cat# 560378 RRID:AB_1645328
Mouse anti-Akt (pS473)	Cell Signaling Technology	Clone: N/A Cat# 9271 RRID N/A
Anti-Goat Alexa647	Thermo Fisher Scientific	Clone: N/A; Cat# A21447; RRID: AB_141844

REAGENT or RESOURCE	SOURCE	IDENTIFIER
pFoxo1 (S256)	Cell Signaling Technology	Clone: N/A; Cat# 9461; RRID: AB_329831
Phospho-S6 Ribosomal Protein (Ser235/236)-Alexa647	Cell Signaling Technology	Clone: D57.2.2E; Cat# 4851; RRID: AB_916160
Foxo1	Cell Signaling Technology	Clone: C29H4; Cat# 2880S; RRID: AB_2106495
Anti-Rabbit HRP	Cell Signaling Technology	Clone: N/A; Cat# 7074S; RRID: N/A
Anti-Rabbit PE	Jackson ImmunoResearch Laboratories	Clone: N/A; Cat# 111–116-144; RRID: AB_2337985
Anti-Rabbit Alexa647	Jackson ImmunoResearch Laboratories	Clone: N/A; Cat# 111–607-003; RRID: AB_2338084
Anti-mouse PPARγ Alexa647	Santa Cruz Biotechnology	Clone: E-8; Cat# Sc7273;
PPARγ (C26H12) Rabbit mAb	Cell Signaling Technology	Clone C26H12, Cat# 2435
β-Tubulin Ab	Cell Signaling Technology	Clone: N/A; Cat#2146S
TATA-binding protein (TBP) Ab	Cell Signaling Technology	Clone: N/A; Cat#8515S
inVivoMAb anti-mouse PD-1	BioxCell	Cat# BE0146 Clone RMPI 14 RRID: RRID:AB_10949053
Chemicals, Peptides, and Recombinant Proteins		
GW9662	Cayman Chemical	Cat# 70785
TZD	Cayman Chemical	Cat# 71740
Orlistat	Cayman Chemical	Cat# 10005426
Etomoxir	Cayman Chemical	Cat# 11969
AS1842856	Sigma Aldrich	Cat# 344355
AKTi	Cayman Chemical	Cat# 14870
SC-79	Sigma Aldrich	Cat# SML0749
FTY720	Sigma Aldrich	Cat# SML0700
PF-543	Calbiochem	Cat# 567741
W146	Cayman Chemical	Cat# 10009109
JTE-013	Cayman Chemical	Cat# 10009458
S1P	Avanti Polar Lipids	Cat# 860662
Oleic Acid	Sigma	Cat# O3008
BODIPY 493/503	Thermo Fisher Scientific	Cat# D3922
BODIPY 558/568 C_{12}	Thermo Fisher Scientific	Cat# D38835
2-Deoxy-D-glucose (2DG)	Sigma Aldrich	Cat# D6134
Antimycin A	Sigma Aldrich	Cat# A8674
Rotenone	Sigma Aldrich	Cat# R8875
Oligomycin	Sigma Aldrich	Cat# O4876
FCCP	Sigma Aldrich	Cat# C2920
IMDM	GE Healthcare, HyClone	Cat# SH30228.01
RPMI-1640 (Glucose free)	Thermo Fisher Scientific	Cat# 11879–020
Penicillin-Streptomycin	Corning	Cat# 30–001-CI
Fetal Bovine Serum (FBS)	Atlanta Biologicals	Cat# S11150
rIL12	Biolegend	Cat# 577004
rIL6	Biolegend	Cat# 575704
rTGFβ	Biolegend	Cat# 580702

REAGENT or RESOURCE	SOURCE	IDENTIFIER
rhIL2	NCI, Biological Resources Branch	https://ncifrederick.cancer.gov/research/brb/productDataSheets/cytokineHumanInterleukins/IL-2Bulk.aspx
Foxp3 / Transcription Factor Staining Buffer Set	Thermo Fisher Scientific	Cat# 00–5523
Fixation/Permeabilization Solution Kit	BD Biosciences	Cat# 554714
hgp100$_{25–33}$ peptide (KVPRNQDW)	Genscript	Cat# RP20344
Nucleofector Kits for Mouse T Cells	Lonza	Cat# VPA-1006
RIPA Lysis Buffer	Thermo Fisher Scientific	Cat# 89900
NE-PER Nuclear and Cytoplasmic Extraction Reagents	Thermo Fisher Scientific	Cat# 78833
rIL12	Biolegend	Cat# 577004
Critical Commercial Assays		
CellTrace CFSE Cell Proliferation Kit	Thermo Fisher Scientific	Cat# C34554
TransAM® FKHR (FOXO1) Transcription Factor ELISA Kits	Active Motif	Cat# 46396
PPAR 96-Well Strip Plate	Cayman Chemical	Cat#10006887
Triglycerides Reagent	ThermoFisher Scientific	Cat# TR22421
Total Cholesterol Reagents	ThermoFisher Scientific	Cat# TR13421
Adenosine 5′-triphosphate (ATP) Bioluminescent Assay Kit	Sigma	Cat# FLAA-1KT
iScript cDNA Synthesis Kit	Biorad	Cat# 1708891
SsoAdvanced Universal SYBR® Green Supermix	Biorad	Cat# 1725274
Deposited Data		
RNA-seq	This Paper	Accession number GSE129489
Mouse qPCR primers: Oligonucleotide Sequences (5′–3′)		
Cpt1a Forward TCTATGAGGGCTCGCG	This Paper	N/A
Cpt1a Reverse CGTCAGGGTTGTAGCA	This Paper	N/A
IL23r Forward TTCAGATGGGCATGAATGTTTCT	This Paper	N/A
IL23r Reverse CCAAATCCGAGCTGTTGTTCTAT	This Paper	N/A
Csf2 Forward GGCCTTGGAAGCATGTAGAGG	This Paper	N/A
Csf2 Reverse GGAGAACTCGTTAGAGACGACTT	This Paper	N/A
IL22 Forward ATGAGTTTTTCCCTTATGGGGAC	This Paper	N/A
IL22 Reverse GCTGGAAGTTGGACACCTCAA	This Paper	N/A
IL9 Forward CATCAGTGTCTCTCCGTCCCAA CTGAT	This Paper	N/A
IL9 Reverse GATTTCTGTGTGGCATTGGTCAG	This Paper	N/A
Lef1 Forward CTCGTCGCTGTAGGTGATGA	This Paper	N/A
Lef1 Reverse AAATGGGTCCCTTTCTCCAC	This Paper	N/A
Nanog Forward GCAAGAATAGTTCTCGG GATGAA	This Paper	N/A
Nanog Reverse TCTTCCTGGTCCCCACAGTTT	This Paper	N/A
Sphk1 Forward ATGGAACCAGTAGAATGCCCT	This Paper	N/A
Sphk1 Reverse TCCGTTCGGTGAGTAT CAGTTTA	This Paper	N/A
Tcf7 Forward GTGGACTGCTGAAATGTTCG	This Paper	N/A
Tcf7 Reverse AGCATCCGCAGCCTCAAC	This Paper	N/A

REAGENT or RESOURCE	SOURCE	IDENTIFIER
β-actin Forward ACGTAGCCATCCAGG CTGGTG	This Paper	N/A
β-actin Reverse TGGCGTGAGGGAGAGCAT	This Paper	N/A
Experimental Models: Cell Lines		
B16-F10	ATCC	CRL-6475
B16-F10-A2^{+}	Rolf Kiessling, Karolinska Institute, Stockholm, Sweden. *Mycoplasma* testing was done in Mehrotra lab.	N/A
Experimental Models: Organisms/Strains		
C57BL/6	Jackson Laboratory	Stock# 000664
C57BL/6-Tg(HLA-A2.1)1Enge/J	Jackson Laboratory	Stock# 003475
B6.129S7-*Rag1*^{tm1Mom}/J	Jackson Laboratory	Stock# 002216
B6.Cg-Thy1a/Cy Tg(TcraTcrb)8Rest/J	Jackson Laboratory	Stock# 005023
PPAR$\gamma^{fl/fl}$CD4^{cre}	Robert B Clark, University of Connecticut Health Center	Wohlfert et al., 2007
Software and Algorithms		
FlowJo 10.2	TreeStar, OR	https://www.flowjo.com/solutions/flowjo/downloads/
Prism 8	GraphPad	https://www.graphpad.com/scientific-software/prism/
Agilent Seahorse Wave 2.4	Agilent	https://www.agilent.com/en-us/products/cell-analysis-(seahorse)/seahorse-wave-software
CFX Manager 3.1	Biorad	http://www.bio-rad.com/en-us/sku/1845000-cfx-manager-software?ID=1845000